

**NAVAL POSTGRADUATE SCHOOL**  
**Monterey, California**



**DISSERTATION**

**LOW ALTITUDE  
OPTICAL SIGNAL PROPAGATION  
OVER THE OCEAN  
(VOL. I)**

by

Lean-Weng Yeoh

March, 1997

Dissertation Supervisor:

Hung-Mou Lee

Approved for public release; distribution is unlimited.

DTIC QUALITY INSPECTED 8

19971121 131

REPORT DOCUMENTATION PAGE			Form Approved OMB No. 0704-0188	
Public reporting burden for this collection of information is estimated to average 1 hour per response, including the time for reviewing instruction, searching existing data sources, gathering and maintaining the data needed, and completing and reviewing the collection of information. Send comments regarding this burden estimate or any other aspect of this collection of information, including suggestions for reducing this burden, to Washington Headquarters Services, Directorate for Information Operations and Reports, 1215 Jefferson Davis Highway, Suite 1204, Arlington, VA 22202-4302, and to the Office of Management and Budget, Paperwork Reduction Project (0704-0188) Washington DC 20503.				
1. AGENCY USE ONLY (Leave blank)		2. REPORT DATE 1997, March		3. REPORT TYPE AND DATES COVERED PhD. Dissertation
4. TITLE AND SUBTITLE LOW ALTITUDE OPTICAL SIGNAL PROPAGATION OVER THE OCEAN (VOL. I)			5. FUNDING NUMBERS	
6. AUTHOR(S) Lean-Weng Yeoh				
7. PERFORMING ORGANIZATION NAME(S) AND ADDRESS(ES) Naval Postgraduate School Monterey CA 93943-5000			8. PERFORMING ORGANIZATION REPORT NUMBER	
9. SPONSORING/MONITORING AGENCY NAME(S) AND ADDRESS(ES)			10. SPONSORING/MONITORING AGENCY REPORT NUMBER	
11. SUPPLEMENTARY NOTES The views expressed in this thesis are those of the author and do not reflect the official policy or position of the Department of Defense or the U.S. Government.				
12a. DISTRIBUTION/AVAILABILITY STATEMENT Approved for public release; distribution is unlimited.			12b. DISTRIBUTION CODE	
13. ABSTRACT (maximum 200 words) The effects of ocean surface waves on optical signal fluctuations and optical refraction are evaluated. The effects on signal fluctuations were inferred from the ocean surface wave spectral density and temperature fluctuation spectral density. The effects of ocean waves on optical refraction are manifested in the near-surface gradient of the temperature profile. A modified temperature profile incorporating a statistical mixing length scale is proposed. The research points to the importance of certain parameters that should be considered when optical signals skim the ocean surface.				
14. SUBJECT TERMS Refraction, Ocean Waves, Temperature Profile			15. NUMBER OF PAGES 103	
			16. PRICE CODE	
17. SECURITY CLASSIFICATION OF REPORT Unclassified	18. SECURITY CLASSIFICATION OF THIS PAGE Unclassified	19. SECURITY CLASSIFICATION OF ABSTRACT Unclassified	20. LIMITATION OF ABSTRACT UL	

NSN 7540-01-280-5500

Standard Form 298 (Rev. 2-89)  
Prescribed by ANSI Std. Z39-18 298-102



Approved for public release; distribution is unlimited.

**LOW ALTITUDE  
OPTICAL SIGNAL PROPAGATION  
OVER THE OCEAN**

Lean-Weng Yeoh  
Ministry of Defence, Singapore  
M.S., Naval Postgraduate School, 1990  
E.E., Naval Postgraduate School, 1990

Submitted in partial fulfillment of the requirements for the degree of  
**DOCTOR OF PHILOSOPHY IN ELECTRICAL ENGINEERING**

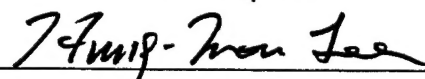
from the

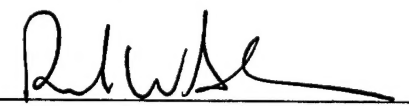
**NAVAL POSTGRADUATE SCHOOL  
March 1997**

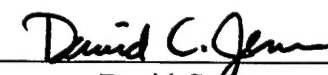
Author:


  
Lean-Weng Yeoh

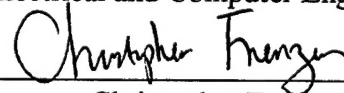
Approved by:

  
Hung-Mou Lee  
Associate Professor of Electrical and Computer Engineering,  
Dissertation Supervisor

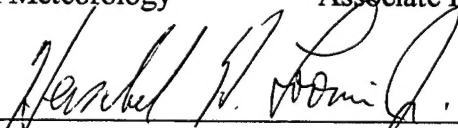
  
Richard W. Adler  
Senior Lecturer of  
Electrical and Computer Engineering

  
David C. Jenn  
Associate Professor of  
Electrical and Computer Engineering

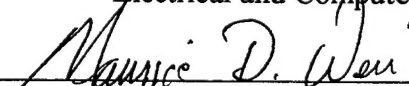
  
Kenneth L. Davidson  
Professor of Meteorology

  
Christopher Frenzen  
Associate Professor of Mathematics

Approved by:

  
Herschel H. Loomis, Jr., Chair, Department of  
Electrical and Computer Engineering

Approved by:

  
Maurice D. Weir, Assoc. Provost for Instruction



## **ABSTRACT**

The effects of ocean surface waves on optical signal fluctuations and optical refraction are evaluated. The effects on signal fluctuations were inferred from the ocean surface wave spectral density and temperature fluctuation spectral density. The effects of ocean waves on optical refraction are manifested in the near-surface gradient of the temperature profile. A modified temperature profile incorporating a statistical mixing length scale is proposed. The research points to the importance of certain parameters that should be considered when optical signals skim the ocean surface.



## TABLE OF CONTENTS

I. INTRODUCTION .....	1
A. BACKGROUND .....	1
B. OBJECTIVES OF THE RESEARCH .....	2
C. ANALYSIS APPROACH .....	3
II. EXPERIMENTAL SET-UP .....	5
A. OPTICAL LINK .....	5
B. FLUX BUOY .....	9
C. ENVIRONMENTAL INFLUENCE AND LIMITATIONS .....	12
III. RAY TRACING .....	15
IV. OCEAN WAVE SPECTRAL ANALYSIS .....	23
A. MEASUREMENT APPROACH .....	23
B. ANALYSIS OF OCEAN SURFACE DISPLACEMENT .....	26
V. BULK AERODYNAMICAL METHOD .....	29
VI. RESULTS OF DATA ANALYSIS .....	35
A. OCEAN SURFACE WAVE SPECTRA AND WAVE HEIGHTS .....	35



B.	TEMPERATURE SPECTRAL DENSITY .....	37
C.	OPTICAL SIGNAL FLUCTUATIONS .....	40
1.	Log-normal Distributions .....	40
2.	Log-normal Variance and Mean .....	46
D.	EFFECTS OF OCEAN SURFACE WAVES ON OPTICAL SIGNAL FLUCTUATIONS .....	49
E.	OPTICAL SIGNAL MODULATION BY OCEAN SURFACE WAVES .....	61
F.	NEAR-SURFACE MEAN GRADIENTS .....	63
G.	EFFECTS OF OCEAN SURFACE WAVES ON THE INDEX OF REFRACTION .....	66
VII. CONCLUSIONS AND RECOMMENDATIONS .....		73
APPENDIX A. OPTICAL SIGNAL SAMPLES .....		77
APPENDIX B. MIXING LENGTH HYPOTHESIS .....		81
LIST OF REFERENCES .....		89
INITIAL DISTRIBUTION LIST .....		91

## ACKNOWLEDGMENTS

I would like to thank my dissertation supervisor, Professor Hung-Mou Lee for his professional guidance throughout the entire period of my research. I would also like to express my appreciation to Professor Richard W. Adler and Professor David C. Jenn for their interest, support and constructive suggestions to my research. Special thanks to Professor Kenneth L. Davidson for his advice on the meteorological aspects of the research. I am thankful to Professor Christopher Frenzen for the helpful discussions on the mathematics of the problem.

I wish to thank the many individuals that contributed to the development of my research: Dr. William Drennan of CCIW for his invaluable suggestions on the analysis of ocean wave spectral density, Dr. Marc Mermelstein of NRL for collaboration of the experiment, Paul Frederickson, Keith Jones and Tamar Neta for their support in the data analysis, Professor Alfred Cooper and William J. Lentz for their helpful discussions and Professor Waldemar Lehn for his ray tracing code.

I am thankful to the Ministry of Defence, Singapore for financial support and giving me the opportunity to pursue this postgraduate studies.

Lastly, I wish to express my gratitude to my wife, Jenny for her unending support, encouragement, love and understanding which enable me to complete my research successfully.

## I. INTRODUCTION

### A. BACKGROUND

The importance of environmental effects on communication links and radar systems has been recognized for the last few decades. Low altitude electromagnetic wave propagation over the ocean is strongly dependent on atmospheric conditions and sea state. It is essential to accurately characterize atmospheric turbulence in order to predict the propagation of electromagnetic signals. For a signal skimming the ocean surface, an understanding of ocean surface wave behavior should be given equal emphasis in electromagnetic wave propagation modeling. Specifically, it is necessary to relate the variation of the index of refraction to atmospheric turbulence and sea state.

The refractive index at optical frequencies can be approximated by

$$n-1 = 77.6(1+7.52 \times 10^{-3} \lambda^{-2})(P/T)10^{-6}, \quad (1)$$

where  $P$  is the atmospheric pressure in millibars,  $T$  is the temperature in Kelvin and  $\lambda$  is the wavelength of light in  $\mu\text{m}$ . To determine the variation in the index of refraction, it is sufficient to know the variation of temperature in the atmospheric surface layer. In the surface layer, the vertical profiles of wind speed,  $u$ , temperature,  $T$  and humidity,  $q$ , all have logarithmic forms  $\xi = (u, T, q)$ , given by [Ref. 1]

$$\xi = \xi_s + \xi_* [\ln(z/z_{0\xi}) - \psi_\xi(\zeta)]/\kappa, \quad (2)$$

where  $\xi_*$  is the flux scaling parameter,  $\xi_s$  is the value at the surface,  $z_{0\xi}$  is the roughness length,  $\kappa$  is the von Karman constant,  $\zeta = z/L$ ,  $L$  the Monin Obukov length and  $\psi_\xi$  the empirically derived stability correction functions.

Equation (2) shows that the model results in large refractive index gradients in regions close to the sea surface. An experiment conducted by the Naval Research Laboratory in June 1994 [Ref. 2] showed that the result of the large index gradient caused rays from the transmitter to be bent more than that required to establish optical continuity between the transmitter and the receiver.

Unlike the atmospheric boundary layer above land, the boundary layer above the sea is continuously interacting with the ocean surface waves. The temperature profile of Equation (2) derived for an immovable surface may not be valid in the region of a few meters above the sea surface. Experimental data on signal heights that commensurate with ocean wave heights demonstrate deviations from the logarithmic distribution given by Equation (2) [Ref. 3].

## **B. OBJECTIVES OF THE RESEARCH**

This research evaluates the effects of ocean surface waves on optical fluctuations and relates the optical refraction to the near-surface gradient of temperature and ocean surface waves. Measurements from an optical link are used to infer the temperature profile and hence the refractive index profile. These are used to assess the effect of the ocean waves. Based on

the experimental data, a proposed temperature profile is used in conjunction with a ray tracing program to validate optical continuity.

### **C. ANALYSIS APPROACH**

The research will first examine the small-scale atmospheric fluctuations due to the presence of the ocean surface waves on the optical signal fluctuations. Computed ocean surface spectral density and air temperature fluctuation spectral density are used to establish the influence of the ocean surface waves. Having established the influence of the ocean waves, modification to the near-surface mean temperature gradients is proposed. This is done by incorporating a random scaling length to account for the random motion of the ocean waves. With the proposed temperature profile, a ray tracing code was used to establish optical continuity between the transmitter and the receiver.

This report comprises two volumes. Volume I contains seven chapters covering the following details: The experimental set-up and instrumented flux buoy are described in Chapter II. Chapter III presents the ray tracing code used in conjunction with the proposed temperature profile to validate optical continuity between the transmitter and the receiver. The analysis of ocean surface wave spectral density is presented in Chapter IV and the bulk aerodynamic method used to analyze the meteorological data is covered in Chapter V. The results of data analysis are presented in Chapter VI. Chapter VII summarizes the findings and recommendations of this research. The complete set of data plots is contained in Volume II.



## II. EXPERIMENTAL SET-UP

### A. OPTICAL LINK

In the experiment, an optical link at  $0.83\text{ }\mu\text{m}$  was set up from Point Pinos at Lat./Long. ( $36^{\circ}38'10.931''\text{N}$ ,  $121^{\circ}55'45.444''\text{W}$ ) to Marina State Beach at Lat./Long. ( $36^{\circ}42'01.365''\text{N}$ ,  $121^{\circ}48'33.651''\text{W}$ ). The propagation path was approximately 12.8 km and the bearing of the transmitter from the receiver was  $237^{\circ}$ . A sketch of the optical path is shown in Figure 1.

The transmitter consists of a  $0.83\text{ }\mu\text{m}$  GaAs laser source with an average power of 35mW and intensity modulated at 4.2 kHz. It has a beam aperture of 50 mm and a beam divergence half angle of 1.3 mrad. The receiver has a 50 mm aperture, a laser line filter with a bandwidth of 40 nm centered at  $0.83\text{ }\mu\text{m}$  followed by an Oriel Instrument Inc. battery operated silicon photodetector and pre-amplifier assembly. Block diagrams of the transmitter and receiver are shown in Figures 2 and 3 respectively. During the experiment, the heights of the transmitter and receiver were varied and the received signal recorded on tape.

The recorded signal was demodulated with a Stanford Research Systems lock-in amplifier with sensitivity set at 50 mV, time constant of 1 ms and internal oscillator set at 4.2 kHz. The output of the lock-in amplifier was connected to a Labview National Instruments 12 bit analog to digital card plugged into a Macintosh computer. The analog signal was sampled at 400 Hz. A total of 41 signal samples covering the period from 30 May 96 to 5 Jun 96 were taken.

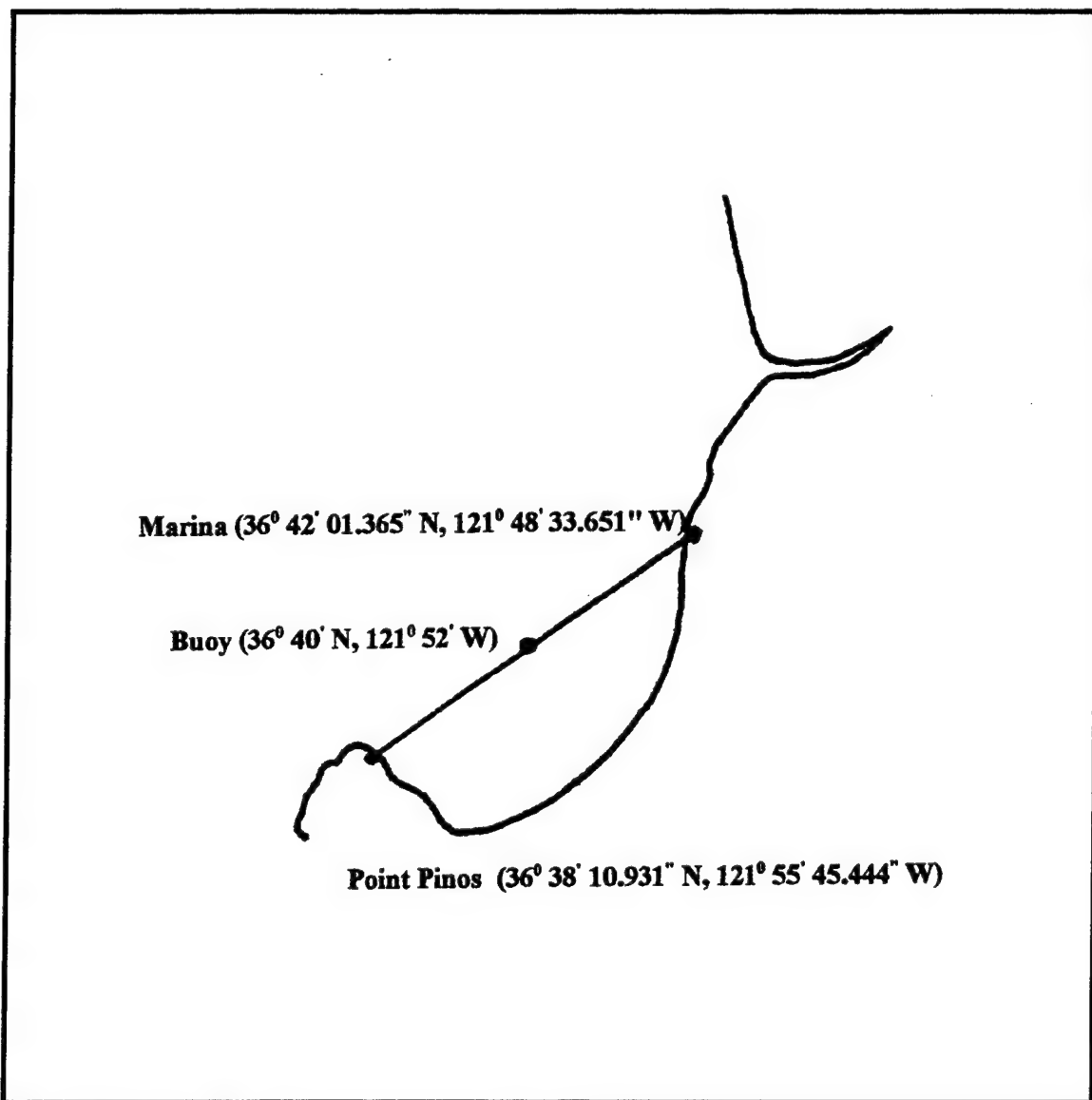


**Figure 1.** Optical Path across the Monterey Bay



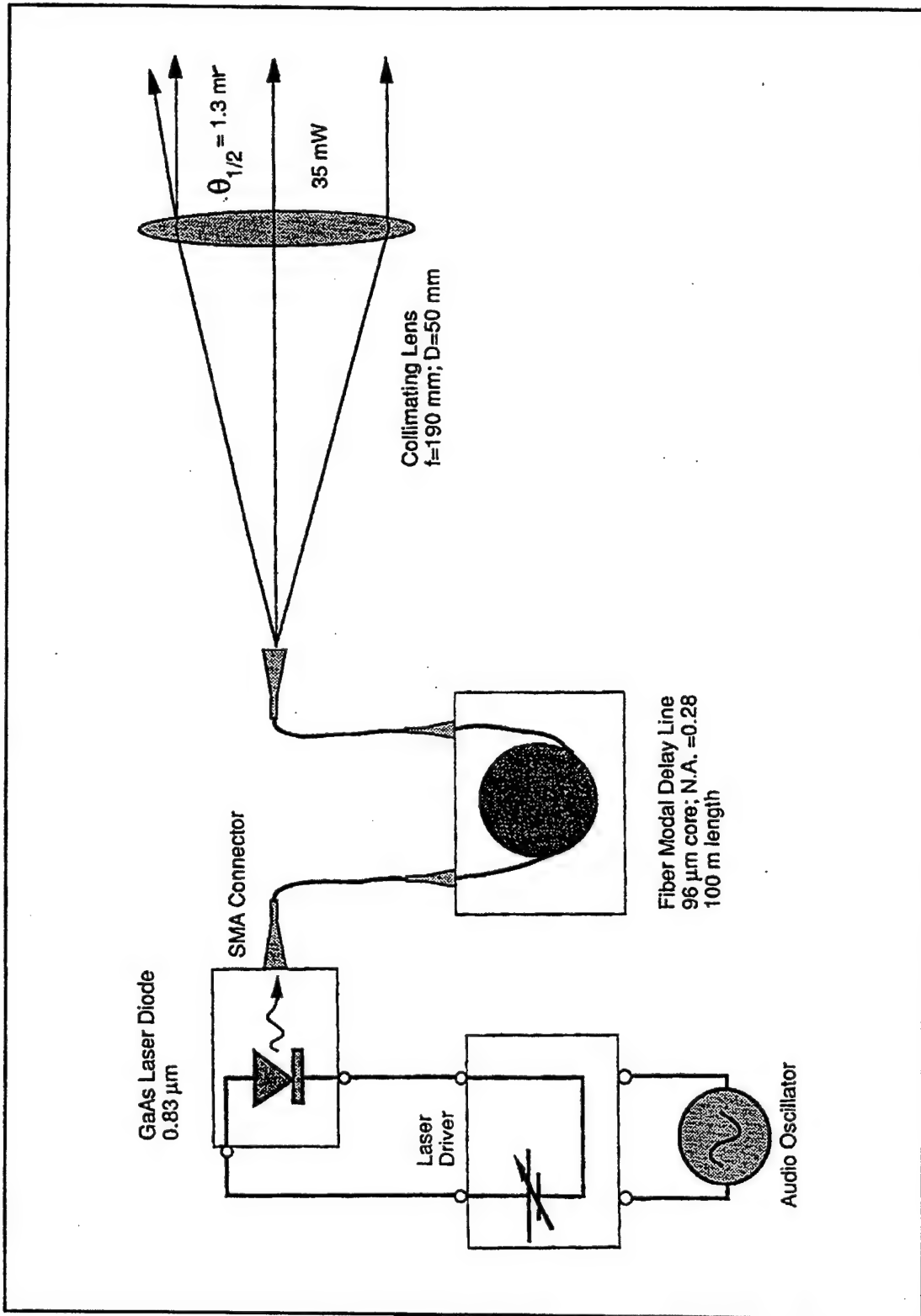


Figure 2. Transmitter Block Diagram

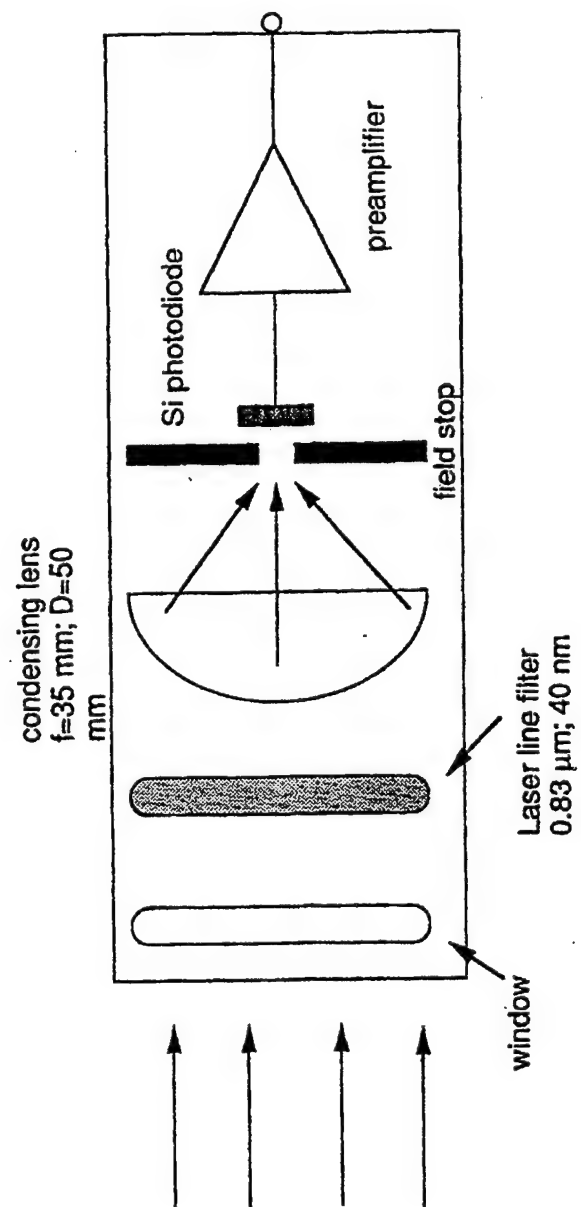


Figure 3. Receiver Block Diagram

## B. FLUX BUOY

The flux buoy was deployed at approximately the mid point of the optical link, at Lat./Long. (36° 40' N, 121° 52' W) where the ocean depth is about 69.5 m. The flux buoy was deployed to record meteorological and wave data. The flux buoy system contains two separate sensor suites, viz., a mean meteorology package and a high frequency sampling 'flux' package. Two sets of data were collected; the high frequency data (flux) of air temperature and wind velocity fluctuations sampled at 21 Hz, wave motion data sampled at 10.5 Hz and low frequency data (mean meteorology) of wind speed, wind directions, humidity, pressure, air and sea temperature sampled at one minute interval. A picture of the buoy is shown in Figure 4.

The high frequency air temperature and velocity were measured by the Solent ultrasonic anemometer at 5.09m above mean tide level. The measurement technique is based on sound pulses transmitted back and forth between transducers. The time of flight in each direction, say  $t_1$  and  $t_2$  are measured. If  $c$  is the speed of sound,  $x$  the distance between the transducers, and there is an air flow  $v$  along the line of the transducers, the following relationships are readily derived:

$$t_1 = \frac{x}{(c+v)} , \quad (3)$$

$$t_2 = \frac{x}{(c-v)} , \quad (4)$$

$$v = 0.5 \times \left[ \frac{1}{t_1} - \frac{1}{t_2} \right] \quad (5)$$

and

$$c = 0.5 \times \left[ \frac{1}{t_1} + \frac{1}{t_2} \right]. \quad (6)$$

By arranging three pairs of transducers in different orientations, the direction and magnitude of the incident air flow may be unambiguously derived. The air temperature is calculated from the speed of sound as follows [Ref. 4]:

$$c^2 = \gamma RT(1+0.51q), \quad (7)$$

where  $\gamma R$  is  $403 \text{ m}^2 \text{ s}^{-2} \text{ K}^{-1}$  for air,  $T$  is the air temperature in degrees Kelvin and  $q$  is the specific humidity in kg of water vapor per kg of air.

The ocean surface wave data was measured by the Systron Donner Motion Pak. The Motion Pak consists of three accelerometers measuring the accelerations of the x, y and z

directions (sway, surge and heave) and three rate gyros measuring the angular rates,  $\theta$ ,  $\phi$  and  $\psi$  (pitch, roll and yaw). The data was sampled at 10.5 Hz. The Motion Pak uses a right-handed coordinate system for the angular rates about the x, y, and z axis. It was mounted so that the x-axis points towards the port side of the buoy, the y-axis points towards the bow and the z-axis downward. The z-axis voltage was adjusted so that when the buoy is at rest on a flat surface, the z-axis linear acceleration voltage output read zero voltage.

Three wave staffs were deployed to measure the high frequency ocean surface waves. The three wave staffs were arranged such that each staff was located at the vertex of an equilateral triangle. The arrangement allows for the computation of the wave directional spectra. Unfortunately, wave staff number 2 was not functioning properly during the experiment.

The buoy's heading relative to magnetic North can be determined from the three Syntron compass outputs. The magnetic deviation from the true North at the buoy was  $15^{\circ} 15'$  East. The buoy's heading relative to the true North can be determined by subtracting the deviation from the buoy magnetic heading.

The low frequency wind speed was measured by the R.M. Young Wind Monitor located at 3.80 m above mean tide level. The wind speed sensor is a helicoid shape propeller molded of polypropylene plastic. Threshold sensitivity of the propeller is 1.0 m/s. Rotation of the propeller produces a linear DC voltage signal directly proportional to the wind speed.

The Everest IR sensor was used to measure the sea surface temperature. The IR radiation from the sea surface is collected by an optical lens system and focussed on an IR

detector. The detector in turn converts the IR signal to an electrical signal proportional to the sea surface temperature.

The low frequency temperature and humidity were measured by the Rhotronics relative humidity and temperature sensor. The humidity sensor is a small hygroscopic capacitor that changes its value as a function of both water vapor pressure and temperature. The temperature sensor uses a platinum 100 ohm resistance temperature device (RTD) to measure air temperature.

The flux data were stored in an Onset Model 6 Toshiba computer with 500 MB of disk storage on board the buoy. Each word is a two-byte data stored as 'big endian' hexadecimals (most significant byte first). The mean meteorology data were stored in another Onset Model 6 computer with 200 MB of disk storage. The data were stored in ASCII format. The bulk aerodynamical method was used to process the mean meteorological data.

### **C. ENVIRONMENTAL INFLUENCE AND LIMITATIONS**

The Monterey Bay has deep water with ocean-like swells. The optical link from Point Pinos to Marina State Beach crosses Monterey Bay where there is relatively very little shoreline influence. The buoy was located at the mid point of the link in the deepest water and farthest from land with open-ocean wind and waves.

The limitation in the deployment of the buoy at a single location leads to the assumption of a spherically stratified atmosphere with a lateral homogeneous refractivity along the path of propagation. This assumption is reasonable only in a well-mixed environment over the ocean.

In the experiment, the spatial average optical measurement is compared with the temporal average meteorological data. In a situation where there is lateral homogeneity along the mean wind direction, the two averages could be considered to be equivalent [Ref. 1].

# FLUX BUOY

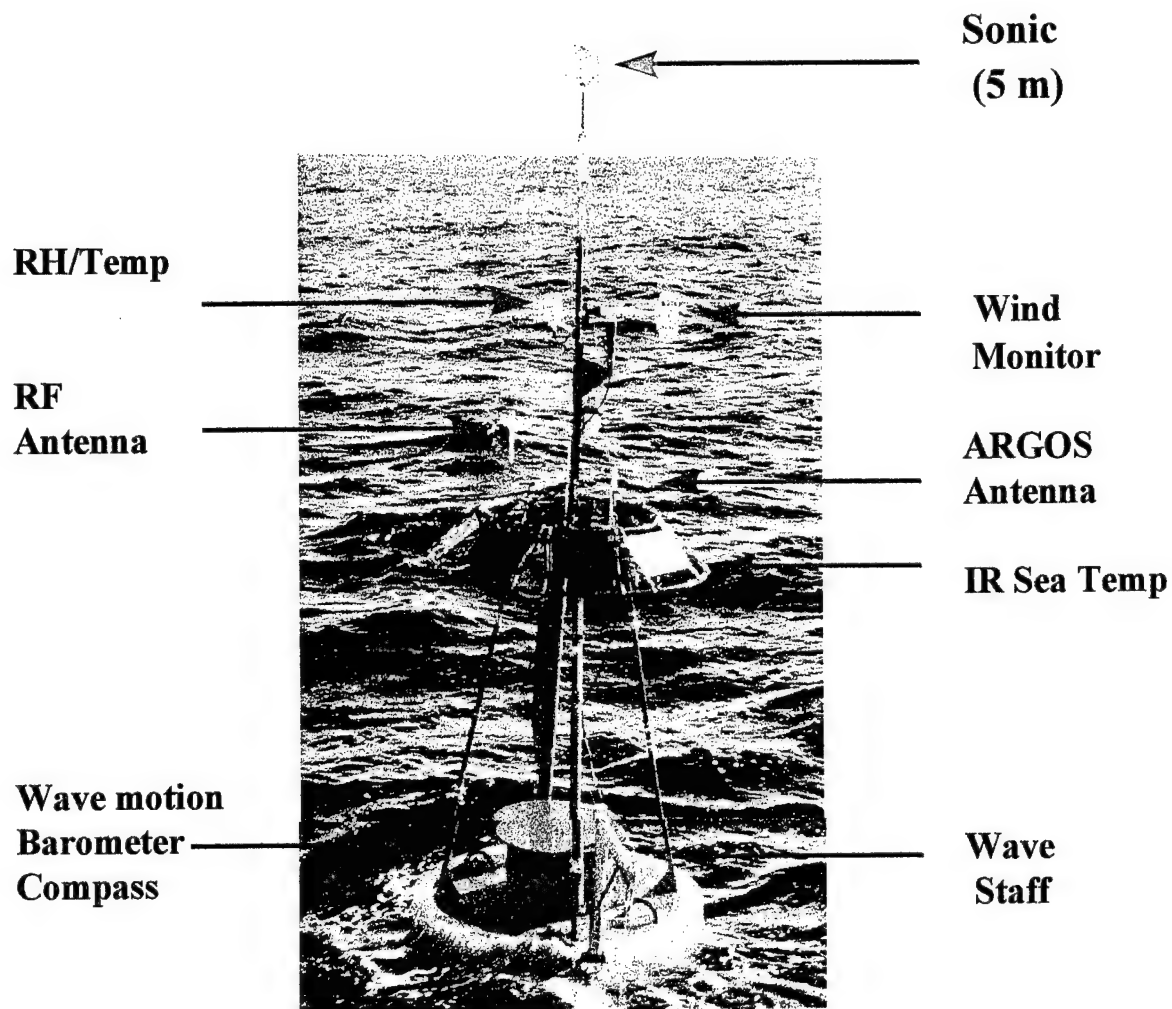


Figure 4. Flux Buoy



### III. RAY TRACING

The ray tracing code was used in conjunction with the standard logarithmic temperature profile and the proposed modified temperature profile to trace rays emanating from the transmitter to the receiver. Optical continuity is said to be achieved if there exists at least one ray above the ocean wave height connecting the transmitter to the receiver.

The ray tracing technique used here is based on the methodology developed by Lehn [Ref. 5]. The model assumes that the atmosphere consists of a number of concentric spherical layers where the temperature is assumed to vary linearly within each layer. In this case, the curvature of a nearly horizontal ray is approximately constant within each layer. Replacement of circular arc by parabolic arc leads to a simpler quadratic expression for the ray trace.

For a ray traversing a stratified atmosphere above a flat earth, Snell's Law dictates that

$$n \sin \theta = A, \quad (8)$$

where  $n$  is the refractive index of the air at any point on the ray,  $\theta$  is the angle between the ray and the vertical, and  $A$  is a constant for the ray.

In rectangular coordinates, the curvature,  $C$ , is given by

$$C = \pm \frac{\frac{d^2z}{dx^2}}{\left[1 + \frac{dz}{dx}\right]^{3/2}}, \quad (9)$$

where  $x$  is the horizontal distance and  $z$  is the elevation above the earth's surface. The slope of the ray is given by

$$\begin{aligned} \frac{dz}{dx} &= \frac{\cos\theta}{\sin\theta} \\ &= \frac{(n^2 - A^2)^{1/2}}{A} \end{aligned} \quad (10)$$

and the second derivative is given by

$$\begin{aligned} \frac{d^2z}{dx^2} &= \frac{d}{dz} \left[ \frac{dz}{dx} \right] \frac{dz}{dx} \\ &= \frac{n}{A^2} \frac{dn}{dz} \end{aligned} \quad (11)$$

With Equations (10) and (11), the ray curvature becomes

$$C = -\frac{\sin\theta}{n} \frac{dn}{dz} \quad (12)$$

The sign in Equation (12) has been chosen so that a positive curvature corresponds to a ray that is concave towards the earth. At optical frequencies, the refractive index of air can be expressed as

$$n = 1 + \frac{\epsilon\beta p}{T}, \quad (13)$$

where  $p$  is the pressure,  $T$  is the absolute temperature in degrees Kelvin,  $\epsilon = 226 \times 10^{-6} \text{ m}^3 \text{ kg}^{-1}$  and  $\beta = 3.48 \times 10^{-3} \text{ J}^{-1} \text{ kg K}$ . Note that Equation (13) is equivalent to Equation (1) when the dependence on wavelength is set at  $\lambda = 0.83 \text{ } \mu\text{m}$  and the pressure expressed in  $\text{N/m}^2$ . The derivative of  $n$  is given by

$$\frac{dn}{dz} = -\frac{\epsilon\beta p}{T^2} \left[ \beta g + \frac{dT}{dz} \right], \quad (14)$$

where the relation  $\beta = \rho p/T$  has been used,  $\rho$  is the density of the air and  $g$  is the acceleration due to gravity. Substituting Equation (14) into the expression for the ray curvature leads to

$$\begin{aligned} C &= \frac{\sin\theta}{n} \frac{\epsilon\beta p}{T^2} \left[ \beta g + \frac{dT}{dz} \right] \\ &= \frac{\epsilon\rho}{(1+\epsilon\rho)} \left[ \beta g + \frac{dT}{dz} \right]. \end{aligned} \quad (15)$$

In ray tracing, the circular arcs that represent the earth's surface, the ray and the layer boundaries are all approximated by parabolic arcs. The coordinate system is shown in Figure 5. The surface of the earth is given by

$$z = -\frac{x^2}{2R}, \quad (16)$$

where  $R$  is the radius of the earth. Similarly a layer located at a height  $h$  above the earth's surface is given by

$$\begin{aligned} z &= -\frac{x^2}{2(R+h)} + h \\ &\approx -\frac{x^2}{2R} + h. \end{aligned} \quad (17)$$

An optical ray with a radius curvature,  $r = I/C$ , starting at  $x = 0$ ,  $z = z_0$  and making an angle of  $\phi_0$  with the horizontal is given by

$$z = -\frac{x^2}{2r} + x \tan \phi_0 + z_0. \quad (18)$$

Within the  $i^{\text{th}}$  layer, the ray path is given by Equation (18) with a radius of curvature  $r_i$ . Ray tracing is performed by determining the intersection of the ray with the layer boundaries. The  $i^{\text{th}}$  layer lies between elevations  $h_{i-1}$  and  $h_i$ . A ray can enter a layer either from above or below and could exit the layer either from top or bottom of the layer. Figure 6 shows a ray entering the  $i^{\text{th}}$  layer from lower boundary. It will proceed to P if  $r_i > R$  or  $r_i < 0$  and to Q if  $r_i$  is positive and sufficiently small. The coordinates of P are found by solving Equations (17) and (18) with  $h = h_i$  in Equation (17) and  $z_0 = h_{i-1}$  in Equation (18). The x-coordinate of P is

$$u_P = \frac{Rr_i}{r_i - R} \left[ -\tan\phi_0 + \left( \tan^2\phi_0 + \frac{2(h_i - h_{i-1})(r_i - R)}{r_i R} \right)^{1/2} \right]. \quad (19)$$

If the discriminant is negative, the intersection P does not exist. Then Q has to be determined.

This is done by letting  $h = h_{i-1}$  in Equation (17). The x-coordinate of Q is

$$u_Q = \frac{2Rr_i \tan\phi_0}{R - r_i} \quad (20)$$

Similarly, for a downward-heading ray, the x-coordinate of P at layer boundary  $h_{i-1}$  is given

by

$$u_P = \frac{Rr_i}{r_i - R} \left[ -\tan\phi_0 - \left( \tan^2\phi_0 - \frac{2(h_i - h_{i-1})(r_i - R)}{r_i R} \right)^{1/2} \right]. \quad (21)$$

Again, a negative discriminant implies that P does not exist and the ray bends upwards and returns to layer boundary  $h_i$  at Q. The x-coordinate of Q is determined from Equation (20).

New coordinates are used each time the ray crosses a layer boundary. Figure 7 shows the case of an upward-heading ray. As the curvature is small, the x-coordinate of the new origin is taken to be  $u_P$ . The layer boundaries can still be described by Equation (17). The elevation angle of the ray is given by

$$\phi_0' = \tan^{-1}m_r - \tan^{-1}m_l, \quad (22)$$

where  $m_r$  and  $m_l$  are the ray and layer slopes respectively at P. The slopes are found by differentiating Equations (17) and (18) giving

$$\begin{aligned} \tan\phi_0' &\approx m_r - m_l \\ &= \tan\phi_0 - \frac{u_P}{r_i} + \frac{u_P}{R}. \end{aligned} \quad (23)$$

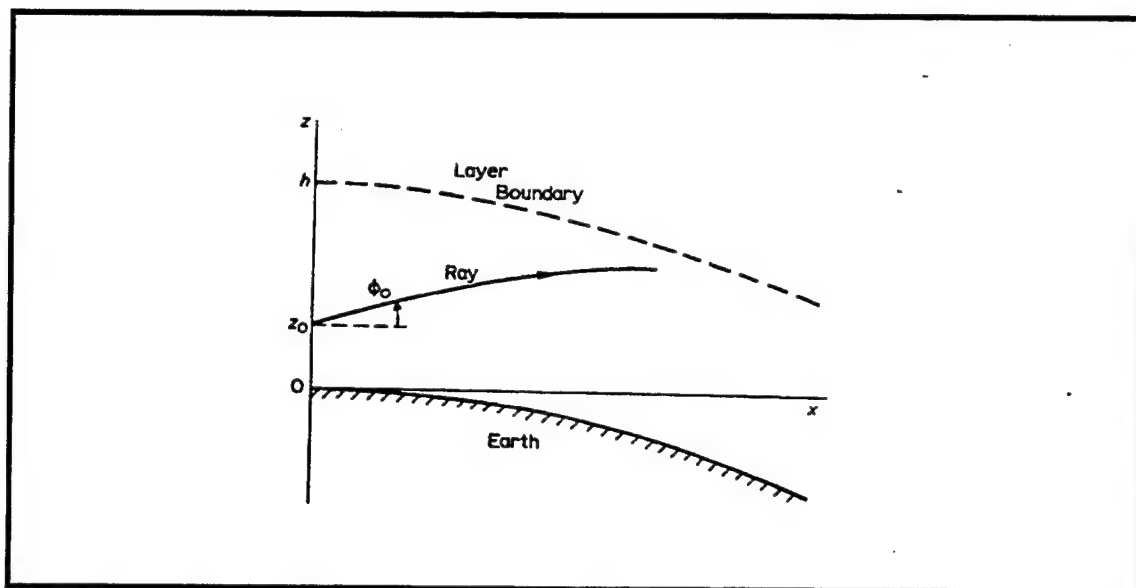


**Figure 5.** Ray Tracing Coordinate System [From Ref. 5]

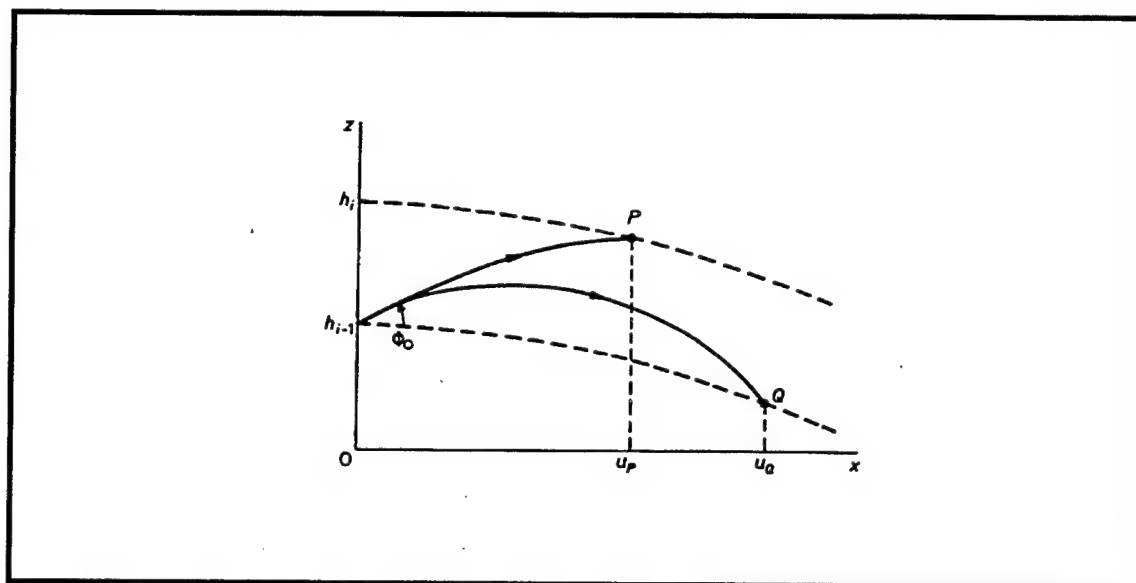


**Figure 6.** Upward-heading Ray in Layer  $i$  [From Ref. 5]

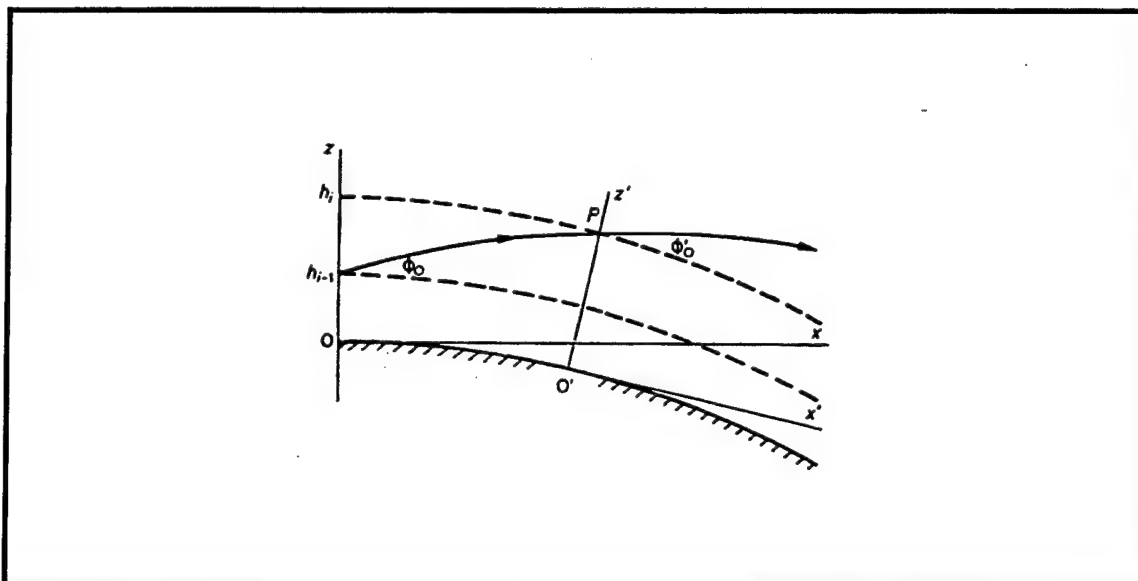


**Figure 7.** Change of Coordinates when the Ray enters a New Layer [From Ref. 5]



## IV. OCEAN WAVE SPECTRAL ANALYSIS

### A. MEASUREMENT APPROACH

In order to establish the possible effects of ocean surface waves on the optical link, it is necessary to examine the ocean surface wave spectra and wave heights at the time when each sample of optical signal was measured. The wave information was collected by the motion pack and wave staff. The motion pack consists of three accelerometers measuring the accelerations of the  $x$ ,  $y$  and  $z$  directions (sway, surge and heave) and three rate gyros measuring the angular rates,  $\theta$ ,  $\phi$  and  $\psi$  (pitch, roll and yaw). The data was sampled at 10.5 Hz.

The true surface displacement is obtained by summing the following three components, viz., the wave height as measured by the wave staff,  $z_m$ , the displacement of the wave staff due to the translational motion of the buoy,  $z_t$ , and the displacement of the wave staff due to the rotational motion between the wave staff and the motion pack [Ref. 6].

As the wave staff and the linear accelerometers were mounted on the moving reference of the buoy, it is necessary to compute the surface displacement in an earth-referenced system. The conversion of the buoy-referenced system to the earth-referenced system can be achieved via a transformation matrix,  $T_{BE}$  [Ref. 7] given by

$$T_{BE} = \begin{bmatrix} \cos\theta \cos\psi & \sin\phi \sin\theta \cos\psi - \cos\phi \sin\psi & \cos\phi \sin\theta \cos\psi + \sin\phi \sin\psi \\ \cos\theta \sin\psi & \sin\phi \sin\theta \sin\psi + \cos\phi \cos\psi & \cos\phi \sin\theta \sin\psi - \sin\phi \cos\psi \\ -\sin\theta & \sin\phi \cos\theta & \cos\phi \cos\theta \end{bmatrix} . \quad (24)$$

If  $\mathbf{a}_B$  represents the translational accelerations measured by the strap-down accelerometers on the buoy, the earth-referenced accelerations,  $\mathbf{a}_E$  are given by

$$\mathbf{a}_E = T_{BE} \mathbf{a}_B + \mathbf{g} , \quad (25)$$

where  $\mathbf{g} = (0, 0, -g)$  is the acceleration due to gravity. The earth-referenced vertical displacement due to the translational motion of the buoy is given by

$$z_{tE} = \int \int [\mathbf{a}_B \cdot (-\sin\theta, \cos\theta \sin\phi, \cos\theta \cos\phi) - g] dt dt . \quad (26)$$

Similarly, the earth-referenced vertical displacement measured by the wave staff is given by

$$z_{mE} = z_{mB} \cos\theta \cos\phi . \quad (27)$$

Finally the displacement due to the rotational motion is determined by integrating the rotational velocity vector,  $\Omega \times T_{BE} L_B$  where  $\Omega$  is the angular velocity of the buoy measured by the rate gyro and  $L_B$  is the distance between the accelerometer and the water surface at the wave staff. The angular velocity,  $\Omega$  is given by

$$\Omega = \begin{bmatrix} -\dot{\theta} \sin\psi + \dot{\phi} \cos\theta \cos\psi \\ \dot{\theta} \cos\psi + \dot{\phi} \cos\theta \sin\psi \\ \psi - \dot{\phi} \sin\theta \end{bmatrix} \quad (28)$$

The vertical displacement due to the rotational motion is given by

$$z_{rE} = \int [L_{E2}(-\dot{\theta} \sin\psi + \dot{\phi} \cos\theta \cos\psi) - L_{E1}(\dot{\theta} \cos\psi + \dot{\phi} \cos\theta \sin\psi)] dt, \quad (29)$$

where

$$L_E = T_{BE} L_B \quad (30)$$

and the subscripts *E1* and *E2* represent the component of the vector.

The true ocean surface displacement is given by

$$z = z_{tE} + z_{mE} + z_{rE} . \quad (31)$$

Once the ocean surface displacement is determined, the rms ocean surface displacement,  $\sigma$  can be computed and the significant wave height,  $H_s$  is given by

$$H_s = 4\sigma . \quad (32)$$

## B. ANALYSIS OF OCEAN SURFACE DISPLACEMENT

The analysis of ocean surface displacement or elevation was carried in the frequency domain using Fourier Transform. The rate gyros do not have good low frequency response and therefore it is necessary to use complementary filtering to patch the low frequency tilt reference of the rate gyros with the linear accelerometers as follows

$$\theta = \theta_{HP} - \sin^{-1}(a_y/g)_{LP} , \quad (33)$$

$$\phi = \phi_{HP} + \sin^{-1}(a_x/g)_{LP} \quad (34)$$

and

$$\psi = \psi_{HP} + \sin^{-1}(com)_{LP} , \quad (35)$$

where  $a_x$  and  $a_y$  represent the observed linear acceleration in the  $x$  and  $y$  direction, the subscripts  $HP$  and  $LP$  represent the high pass and low pass filtered output and  $com$  is the compass output. The first term on the right hand side of Equations (33) to (35) represents the high pass angular motions from the rate gyros which provides the wave-induced angular motions and the second term represents the low frequency tilt reference from the accelerometers. The effect is an all-pass filter which removes the unwanted drift in the rate gyros while retaining the low frequency tilt reference.

To compute  $z_{rE}$  and  $z_{tE}$ , the integration and double integration are done in the frequency domain by dividing the Fourier Transform of  $z_{rE}$  and  $z_{tE}$  with  $(i\omega)$  and  $(i\omega)^2$  respectively. The division by  $\omega$  introduces a singularity at  $\omega = 0$ . However, there is no ocean wave with frequency lower than 0.04 Hz, i.e., 25 second waves, since there is not enough fetch in the ocean to sustain the waves without breaking. The waves in the Atlantic Ocean and Pacific Ocean rarely exceed 20 seconds and 25 seconds respectively [Ref. 8]. The singularity problem is alleviated by performing a high-pass filtering of the wave spectrum at 0.04 Hz. The power spectral density of the ocean surface waves and significant wave height were computed for the duration of time when the optic signal samples were being measured.



## V. BULK AERODYNAMICAL METHOD

The bulk aerodynamical formulations for the fluxes of momentum, sensible heat and latent heat across the air-sea interface and vertical profile estimation are given by

$$\tau = \rho C_D(z)[u(z)-u_s]^2 , \quad (36)$$

$$Q_H = -\rho c_p C_H(z)[u(z)-u_s][T(z)-T_s] \quad (37)$$

and

$$Q_E = -\rho L_e C_E(z)[u(z)-u_s][q(z)-q_s] , \quad (38)$$

where  $\rho$  is the air density,  $c_p$  is the specific heat of air,  $L_e$  is the latent heat of vaporization,  $C_D$ ,  $C_H$  and  $C_E$  are the height dependent bulk transfer coefficients for momentum, sensible heat and latent heat respectively,  $u$ ,  $T$ ,  $q$  are the wind speed, potential temperature and specific humidity respectively,  $z$  is the height above the sea surface and the subscript  $s$  denotes the respective values at the sea surface.

In the atmospheric surface these fluxes can be expressed according to Monin-Obukov

Similarity (MOS) theory scaling parameters as

$$\tau = \rho u_*^2, \quad (39)$$

$$Q_H = -\rho c_p u_* T_* \quad (40)$$

and

$$Q_E = -\rho L_e u_* q_* , \quad (41)$$

where  $u_*$ ,  $T_*$  and  $q_*$  are the MOS surface layer scaling parameters for momentum, temperature and humidity respectively. By combining Equations (36) to (41), these scaling parameters can be defined according to the bulk transfer coefficients as

$$u_* = C_D^{1/2} [u(z) - u_s] , \quad (42)$$

$$T_* = C_H C_D^{-1/2} [T(z) - T_s] \quad (43)$$



and

$$q_* = C_E C_D^{-1/2} [q(z) - q_*] . \quad (44)$$

The bulk transfer coefficients can be defined as

$$C_D(z) = \frac{\kappa^2}{[\ln(z/z_{0u}) - \psi_u(z/L)]^2} , \quad (45)$$

$$C_H(z) = \frac{\kappa^2}{[\ln(z/z_{0u}) - \psi(z/L)][\ln(z/z_{0T}) - \psi_T(z/L)]} \quad (46)$$

and

$$C_E(z) = \frac{\kappa^2}{[\ln(z/z_{0u}) - \psi(z/L)][\ln(z/z_{0q}) - \psi_q(z/L)]} , \quad (47)$$

where  $\kappa$  is the von Karman constant, and  $\psi_u$ ,  $\psi_T$  and  $\psi_q$  are the integrated forms of the dimensionless stability correction functions for wind speed, temperature and specific humidity

respectively, given by

$$\psi_u(z/L) = \begin{cases} 2\ln[(1+x)/2] + \ln[(1+x^2)/2] - 2\tan^{-1}(x) + \pi/2, & z/L < 0 \\ -8z/L, & z/L \geq 0 \end{cases}, \quad (48)$$

$$\psi_T(z/L) = \psi_q(z/L) = \begin{cases} 2\ln[(1+x)/2], & z/L < 0 \\ -7z/L, & z/L \geq 0 \end{cases}, \quad (49)$$

$$x = (1 - 20z/L)^{1/4} \quad (50)$$

and  $z_{0u}$ ,  $z_{0T}$  and  $z_{0q}$  are the roughness lengths for momentum, temperature and humidity respectively. The Obukov length scale,  $L$  is defined as

$$L = \frac{T_v u_*}{[\kappa g (T_* + 0.61 T_{q*})]}, \quad (51)$$

where  $g$  is the acceleration due to gravity and  $T_v$  is the virtual temperature introduced to take into account the effects of humidity:

$$T_v = T(1 + 0.61q) . \quad (52)$$

To determine the vertical profile of wind speed, temperature and specific humidity, iterative computation of  $u_*$ ,  $T_*$ ,  $q_*$ ,  $z_{0u}$ ,  $z_{0T}$ ,  $z_{0q}$  and  $L$  are performed and the vertical profile calculated as

$$u = u_s + \frac{u_*}{\kappa} [\ln(z/z_{0u}) - \psi_u(z/L)] , \quad (53)$$

$$T = T_s + \frac{T_*}{\kappa} [\ln(z/z_{0T}) - \psi_T(z/L)] \quad (54)$$

and

$$q = q_s + \frac{q_*}{\kappa} [\ln(z/z_{0q}) - \psi_q(z/L)] . \quad (55)$$

The temperature profile estimated in this manner was used as input to the ray tracing program to determine if optical continuity between the transmitter and the receiver can be established.

## VI. RESULTS OF DATA ANALYSIS

### A. OCEAN SURFACE WAVE SPECTRA AND WAVE HEIGHTS

The power spectral densities of the ocean surface waves were computed for the duration when the optical signals were being measured. A total of 41 samples were computed. A typical sample of the wave spectrum is shown in Figure 8. It can be seen from the spectrum that the ocean surface waves are dominated by swells with a peak frequency of about 0.1 Hz, i.e. 10 second waves. There are wind generated waves with a peak frequency at about 0.4 Hz, i.e., 2.5 second waves. The spectrum exhibits a high frequency roll-off as  $\omega^{-4}$ . This is the established behavior of the equilibrium range of wind-sea spectra [Ref. 9 ].

The rms wave height,  $\sigma$ , was computed from the power spectral density by the following relation

$$\sigma^2 = \frac{1}{N^2} \sum_{i=1}^N |Z(f)|^2 , \quad (56)$$

where  $Z(f)$  is the Fast Fourier Transform (FFT) of the ocean surface displacement,  $z(t)$  and  $N$  is the sample size. For the 41 samples, the rms wave height ranges from 0.18 m to 0.7 m.

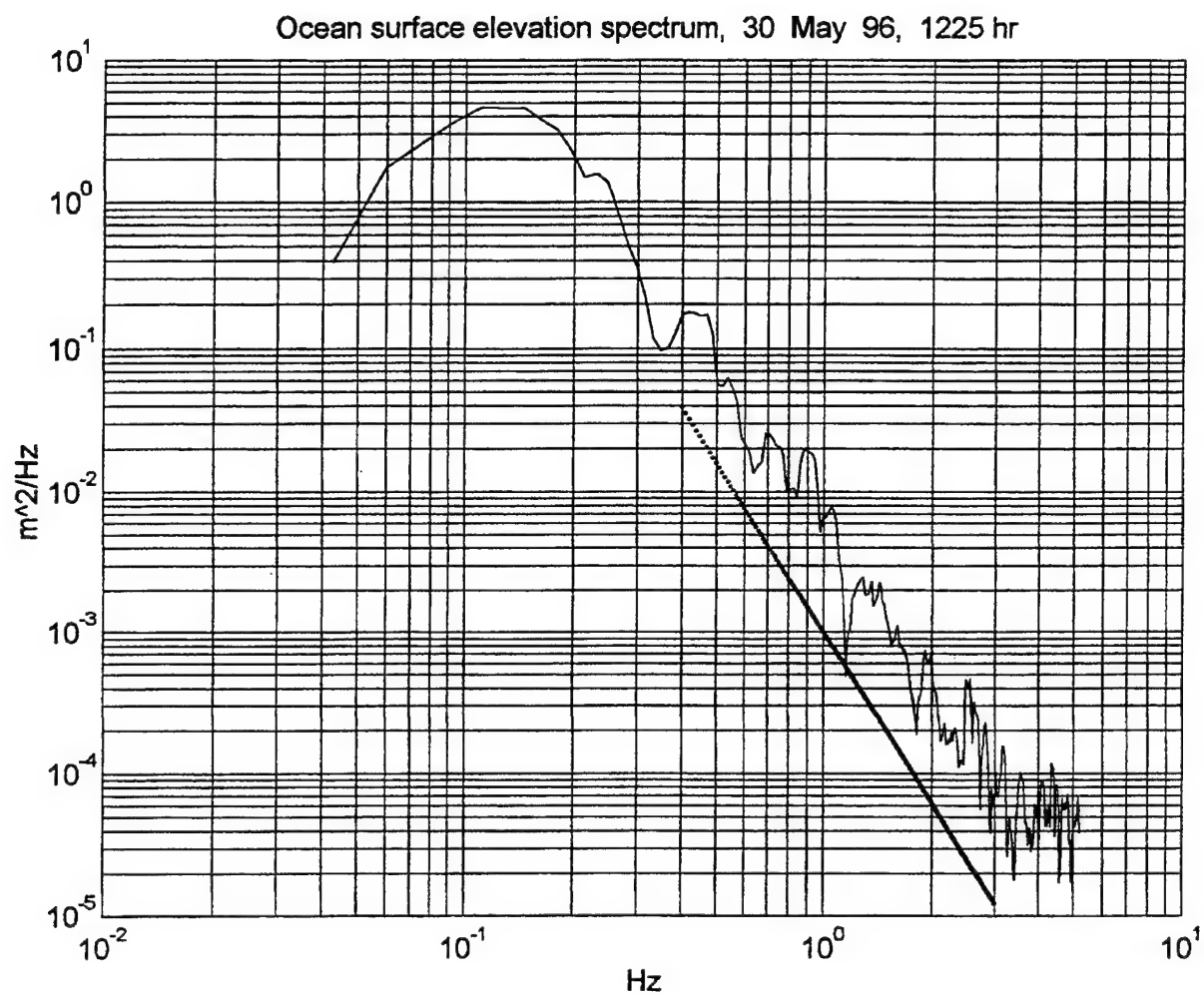


**Figure 8.** Ocean Surface Elevation Spectrum. The straight line represents the -4 slope.

## B. TEMPERATURE SPECTRAL DENSITY

The aspect of atmospheric turbulence of relevance to optical propagation is the variation of the index of refraction or equivalently, the variation of the density of air. Air density depends on pressure and temperature. Pressure fluctuations are rapidly dissipated and their effects are negligible compared to temperature fluctuations. Thus, for optical propagation purposes, temperature fluctuations are used to characterize the optical effects of turbulence.

In the experiment, temperature fluctuations sampled at 21 Hz were measured by the sonic anemometer at 5.09 meters above mean sea level. A typical plot of the power spectral density of temperature fluctuations is shown in Figure 9. The spectrum shows the classical  $-5/3$  slope at high frequencies. This dynamic condition in the high frequency range agrees satisfactorily with theoretical predictions and measurements above land [Ref. 10]. At lower frequencies, the spectrum shows evidence of ocean wave influence. Figure 10 shows the temperature spectral density and corresponding ocean surface spectral density of the wind waves. The spectral density of wind waves was obtained by performing high pass filtering on the swell-dominated wave spectrum, thus removing the swells from the spectrum. It can be seen that the temperature spectrum displays the characteristic spectral density peak at the peak of the corresponding wind wave spectrum indicating the influence of the ocean waves.

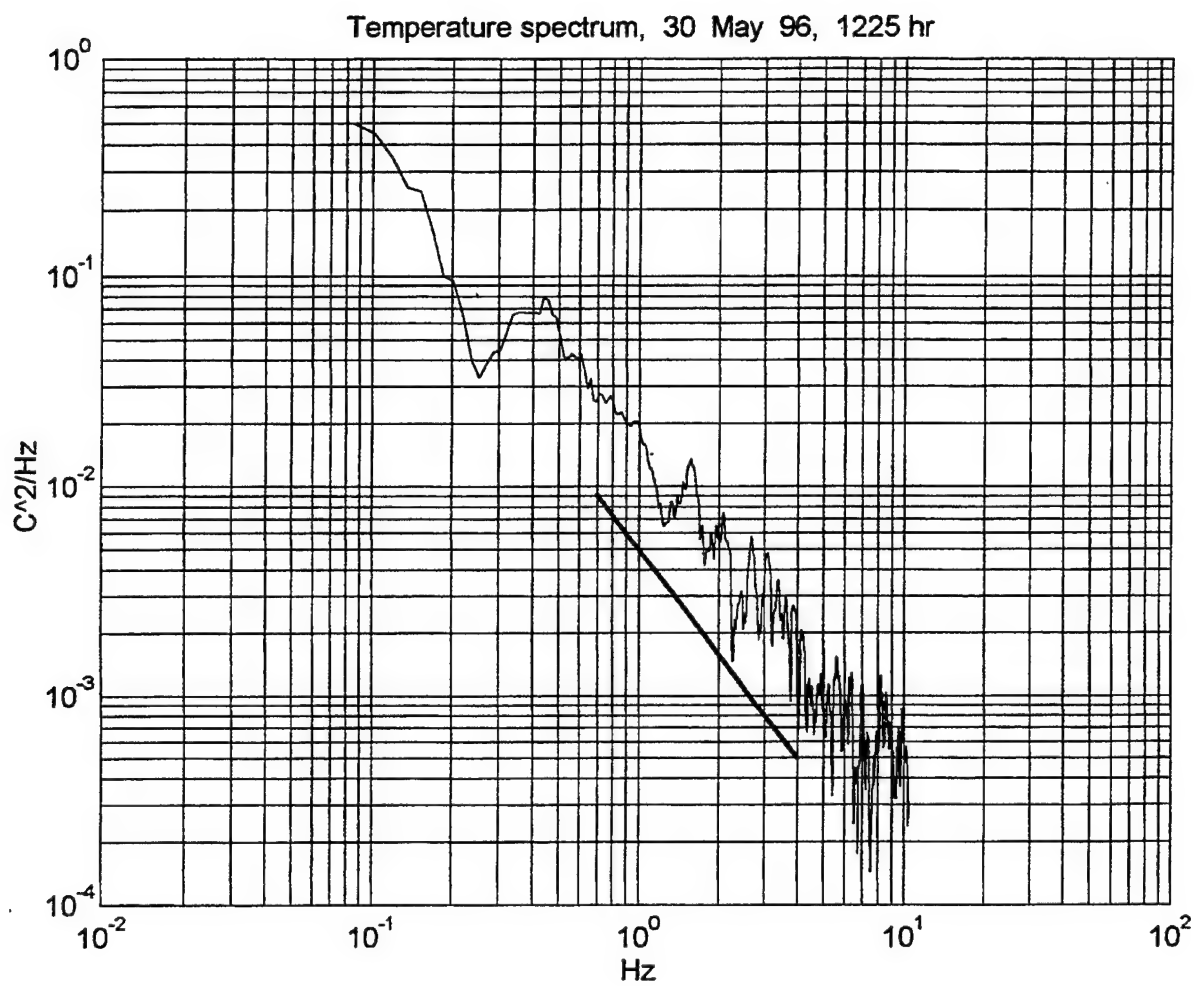


**Figure 9.** Temperature Spectrum. The straight line represents the  $-5/3$  slope.



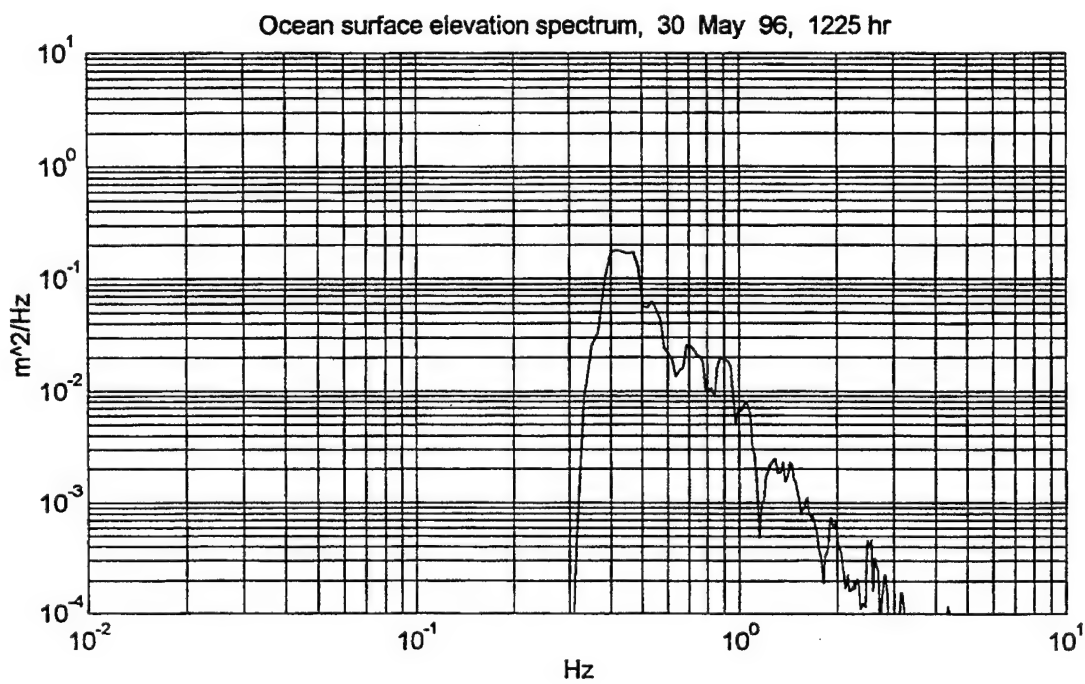
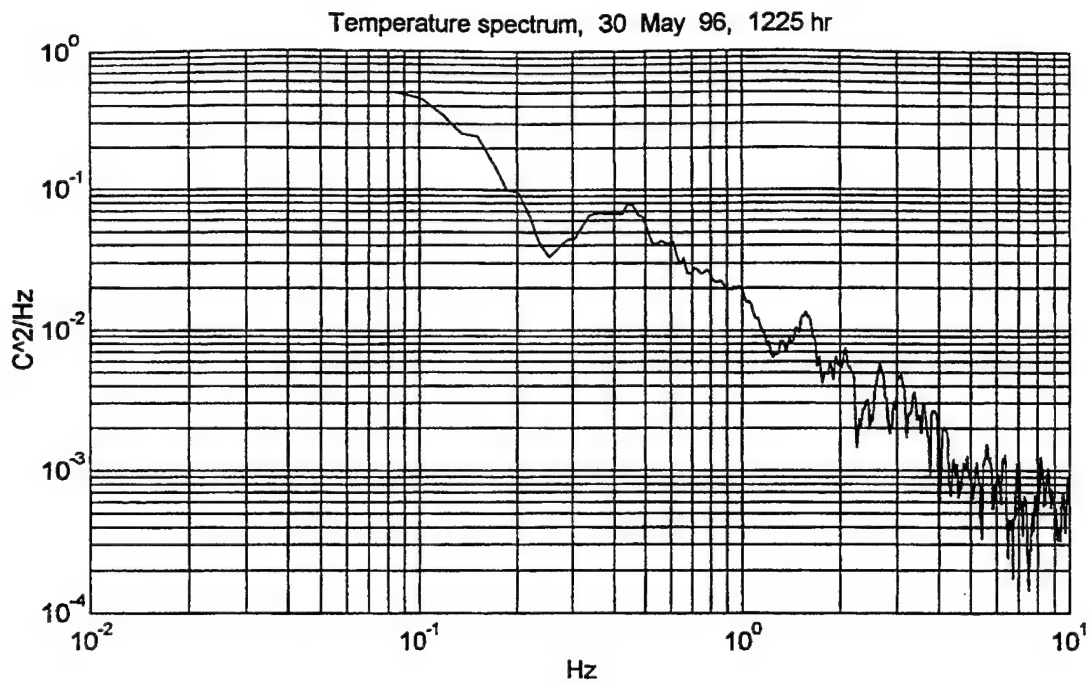


**Figure 10.** Temperature Spectrum and the Corresponding Wind Wave Spectrum.

## C. OPTICAL SIGNAL FLUCTUATIONS

In the analysis of the optical signals, the signal fluctuations are described by the log-normal variance although the variance of the signals can be used as a measure of fluctuations. The research does not attempt to relate the log-normal variance to the saturation phenomenon. The objective is to analyze how the effects of ocean surface waves affect the signal fluctuations per se.

### 1. Log-normal Distributions

To observe the signal fluctuations, a histogram plot of the normalized log intensity (normalized to the mean intensity) was performed for each signal sample. From the histogram plot, it was found that for signal samples where no apparent ocean wave occultation is observed, the intensity fluctuations exhibit a log-normal distribution. For signal samples where wave occultation is evident, deviation from the log-normal distribution results. Typical histogram plots of samples that exhibit log-normal distribution and 'non log-normal distribution' are shown in Figures 11 and 12 respectively.

Log-normal distributed signals are known to exist in signals propagating through random inhomogeneous medium [Ref. 11]. The distribution characteristics are associated with atmospheric radio noise or atmospherics as it is sometimes called. It has been found empirically [ Ref. 12] that the distribution  $P(E > R)$ , where  $E$  is the instantaneous value of HF atmospheric noise and  $R$  is threshold voltage at the receiving point, approaches a Rayleigh distribution for small amplitudes. This is due to the interferences of many mutually overlapping small atmospherics with uniformly distributed phase. However for large

amplitudes, the distribution deviates considerably from the Rayleigh distribution and approaches a log-normal distribution. This is believed to be due to strong atmospherics that do not overlap in time.

The theory of the distribution of peak value of atmospherics can be explained as follows. The peak value of atmospherics,  $E_p$  can be represented by the following expression

$$E_p = \frac{K\sqrt{P_0}}{d} \exp\left(-\sum_{j=1}^n \delta_j d_j\right), \quad (57)$$

where  $P_0$  is the peak power of the atmospheric discharge,  $d$  is the propagation path,  $d_j$  is a section of the propagation path,  $\delta_j$  is the attenuation constant of the  $j^{\text{th}}$  section and  $K$  is a constant. By writing Equation (57) as

$$E_p = e^{\Delta} = \exp\left(-\sum_{j=1}^n \delta_j d_j + \frac{1}{2}\ln P_0 - \ln\sum_{j=1}^n d_j + \ln K\right), \quad (58)$$

the sum of the attenuations of each section,  $\Delta$ , is defined. It is assumed that the fluctuations of  $P_0$  and  $d$  are negligible compared to the first term in the exponential of Equation (58). Thus, only the first term will thus be used to determine the distribution of  $\Delta$ . Since most

atmospherics are propagated from long distances away, it is reasonable to assume that the attenuations  $\delta_j, d_j$  are independent and none of the  $\delta_j, d_j$ 's make a predominant contribution to the sum of the attenuations. Therefore  $\Delta$  is normally distributed with probability density function given by

$$p(\Delta) = \frac{1}{\sigma_{\Delta}\sqrt{2\pi}} \exp\left[-\frac{(\Delta-\mu)^2}{2\sigma_{\Delta}^2}\right] \quad (59)$$

where  $\mu$  is the mean,  $\sigma_{\Delta}^2$  is the variance. From Equation (58) we have

$$\Delta = \ln E_p \quad (60)$$

and substituting Equation (59) into Equation (60), the density function of  $E_p$  is

$$\lambda(E_p) = \frac{1}{\sigma_{\Delta}E_p\sqrt{2\pi}} \exp\left[-\frac{(\ln E_p - \mu)^2}{2\sigma_{\Delta}^2}\right] \quad (61)$$

Equation (61) is the log-normal distribution which has been found experimentally to apply to

the propagation of optical signals through atmospheric turbulence in the absence of occultation of the optical signals by ocean surface waves.

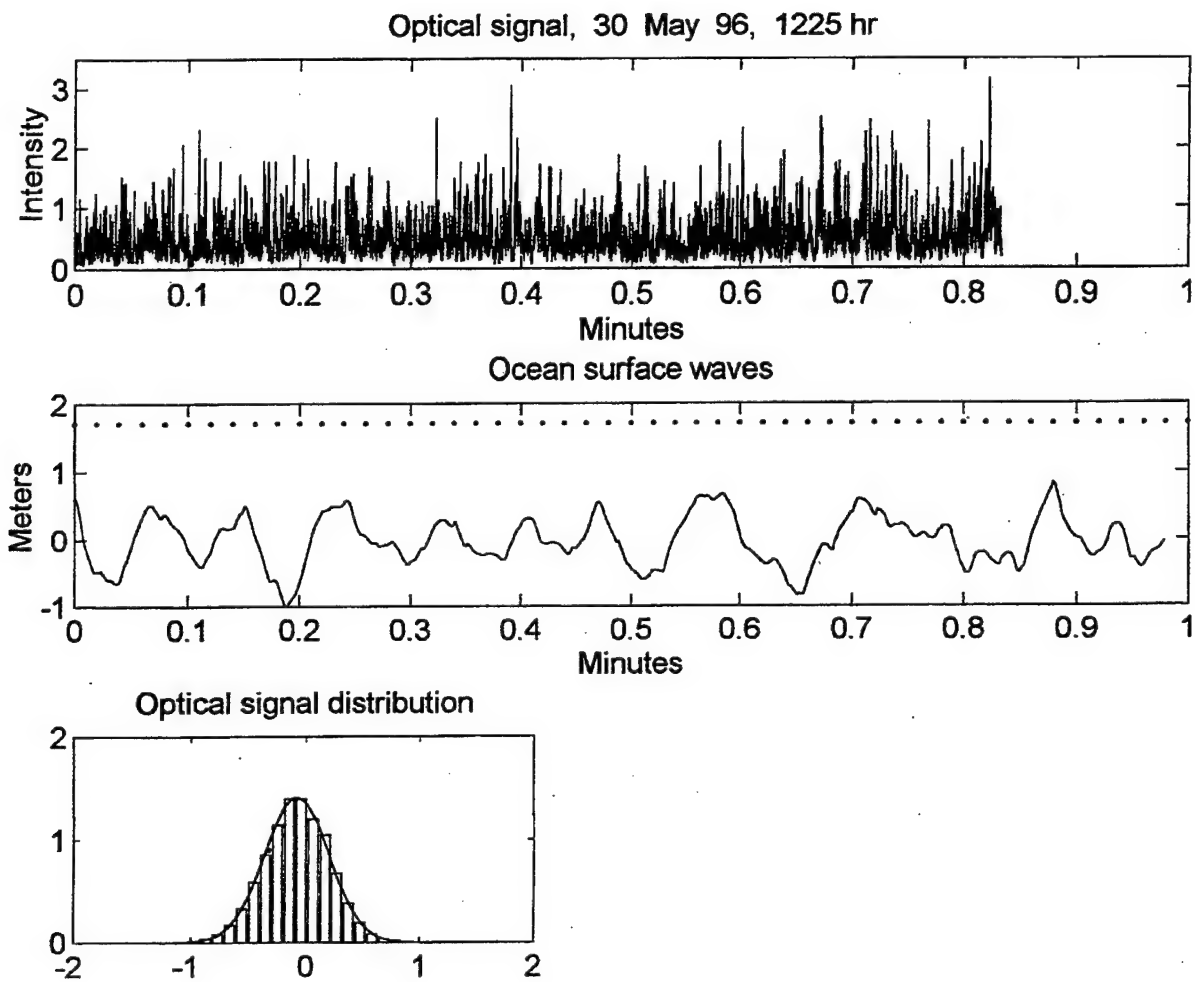


**Figure 11.** Optical Signal Intensity and Distribution Plots and the Corresponding Ocean Waves.

'...' in ocean waves plot indicates height of optical ray path above the waves.

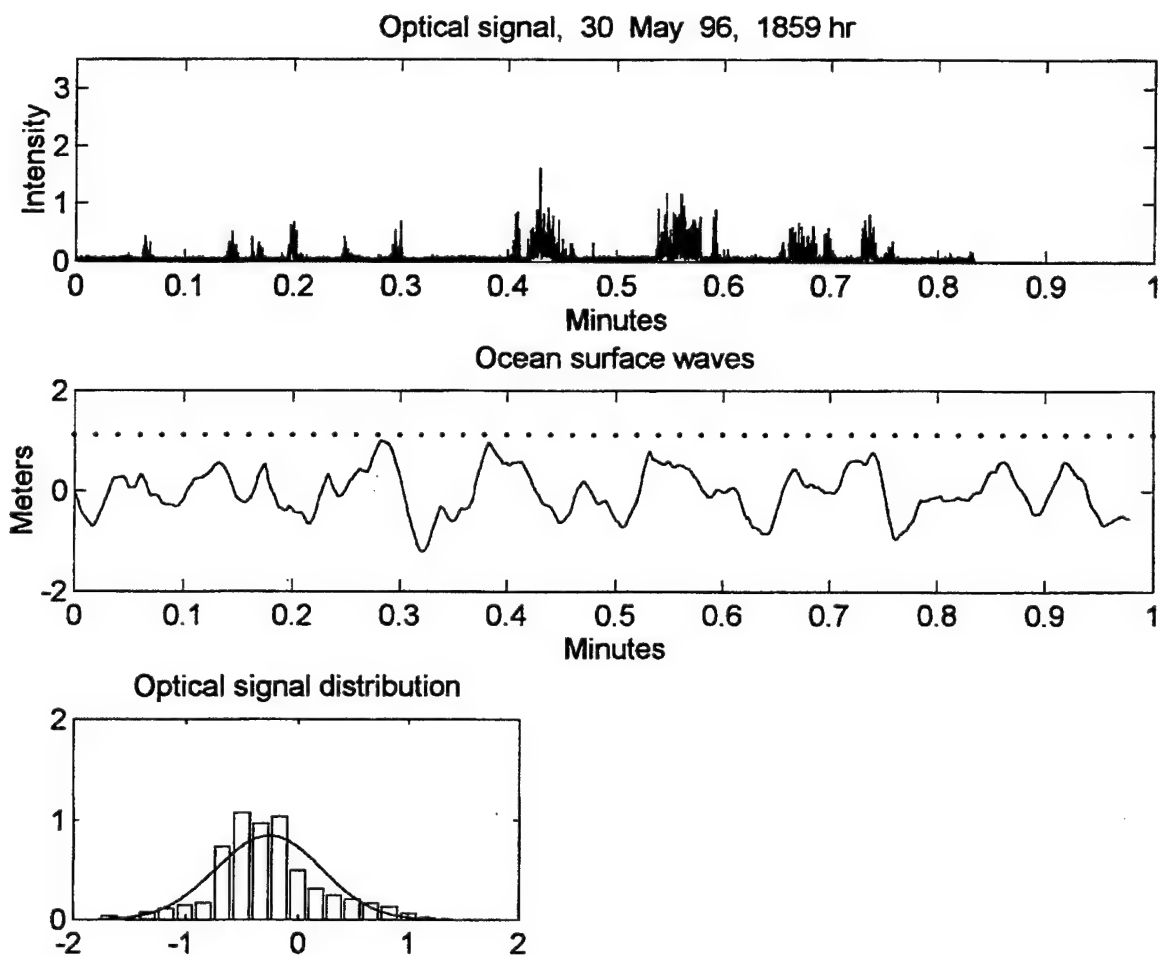


**Figure 12.** Optical Intensity and Distribution Plots and the Corresponding Ocean Waves Plot  
(with Occultation of Optical Signal by Ocean Waves).

## 2. Log-normal Variance and Mean

From the above equations, the relationship between the log-normal mean intensity and log-normal variance can be derived. In general, an electromagnetic wave field  $E(\vec{r}, t)$  can be represented by

$$E(\vec{r}, t) = I(\vec{r})^{1/2} \exp[i\vec{k} \cdot \vec{r} - i\omega t] , \quad (62)$$

where  $\omega$  is the temporal frequency of the electromagnetic field,  $k$  is the propagation vector and  $I(\vec{r})$  is the irradiance or intensity. In the presence of turbulence, Equation (62) becomes

$$E(\vec{r}, t) = \langle I(\vec{r}) \rangle^{1/2} \exp[i\vec{k} \cdot \vec{r} - i\omega t + \chi(\vec{r}, t) + \phi(\vec{r}, t)] , \quad (63)$$

where  $\langle I(\vec{r}) \rangle^{1/2}$  is the average non fluctuating part of the irradiance,  $\chi(\vec{r}, t)$  describes the fluctuating part and  $\phi(\vec{r}, t)$  is the phase variation. The random variables,  $\chi(\vec{r}, t)$  and  $\phi(\vec{r}, t)$  have Gaussian probability distributions. To examine the irradiance fluctuations, the instantaneous irradiance can be written as

$$I(r, t) = \langle I(r) \rangle \exp[2\chi(r, t)] . \quad (64)$$



It follows that  $I(r, t)$  has a log-normal distribution. Taking the average on both sides of Equation (64), and using the relation valid for any real-valued Gaussian random variable,

$$\langle e^{az} \rangle = \exp \left[ a \langle z \rangle + \frac{1}{2} a^2 \sigma^2 \right], \quad (65)$$

Equation (64) becomes

$$\langle I \rangle = \langle I \rangle \exp(2\langle \chi \rangle + 2\sigma_\chi^2). \quad (66)$$

In the presence of turbulence,  $\langle I \rangle$  should be a constant independent of the turbulence. It follows that

$$\langle \chi \rangle = -\sigma_\chi^2. \quad (67)$$

A plot of log normal mean intensity against the log normal variance for those signal samples not occluded by the ocean surface waves in Figure 13 further verifies the log-normal distribution characteristics of the optical signals.

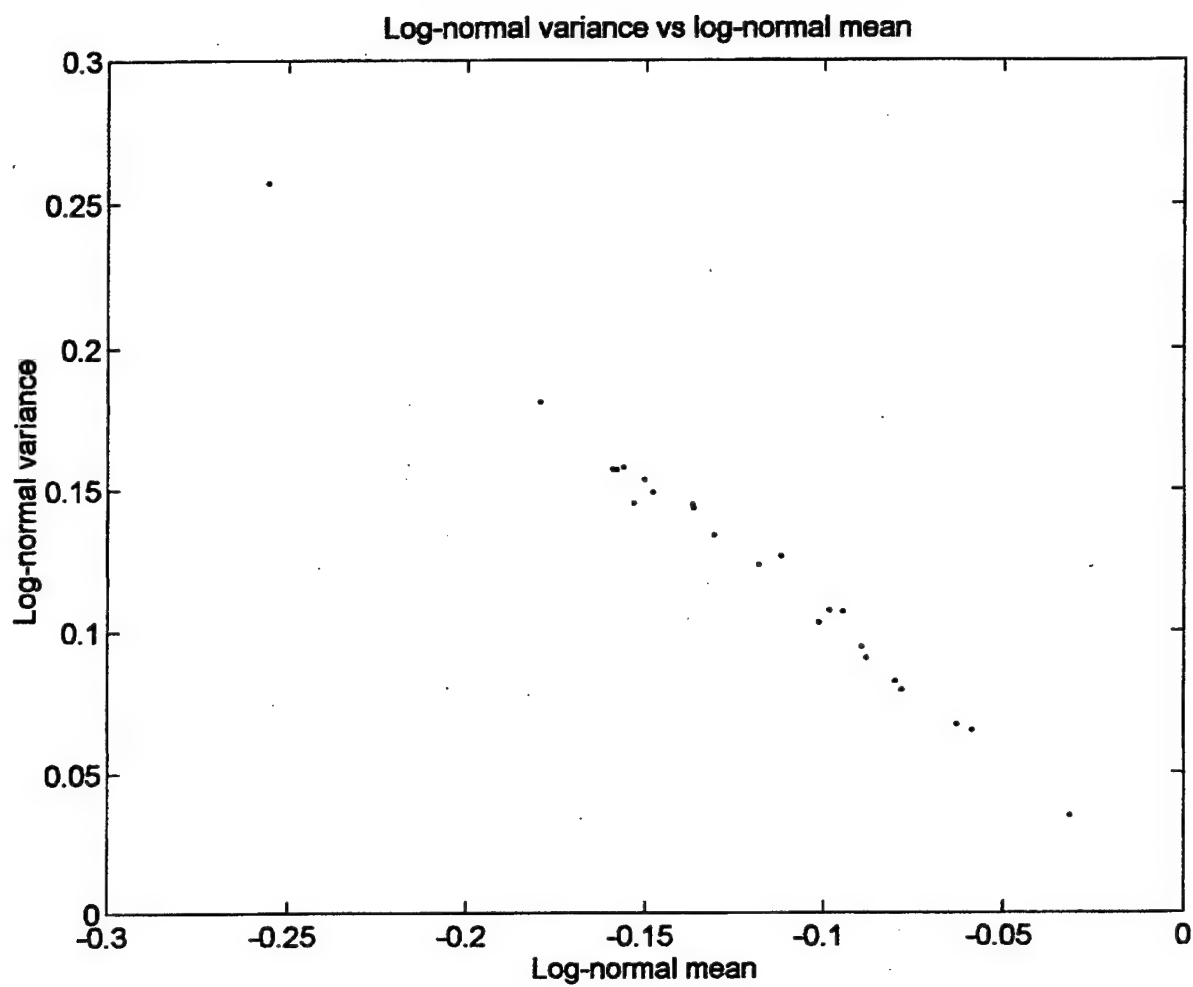


**Figure 13.** Log-normal Variance vs. Log-normal Mean.

#### D. EFFECTS OF OCEAN SURFACE WAVES ON OPTICAL SIGNAL FLUCTUATIONS

Due to the random motion of the ocean waves, it is necessary to establish a way to measure the distance of the ray path above the ocean waves. The method adopted here is to calculate the normalized mean square distance,  $h^2$ , (normalized to the variance of the ocean surface displacement) of the ray path above the ocean waves, given by

$$h^2 = \frac{1}{\sigma^2} \sum_i (z_{ht} - z_i)^2 \quad (68)$$

where  $\sigma^2$  is the variance of the ocean surface displacement,  $z_{ht}$  is the lowest height of the straight line ray path above mean sea level,  $z_i$  is the instantaneous ocean surface displacement and the summation is performed over the duration of the optical signal transmission. A large mean square distance implies a lower probability of the ray path being blocked by the ocean surface waves. The normalized mean square distance is plotted against the log-normal variance of the signals. For sufficiently large mean square distance, i.e., for the mean square distance greater than 35, the variance of the optical signal increases as the mean square distance decreases. Those signal samples with lower mean square distance also display the same trend but with increased variability, i.e., the signal sample points are widely scattered. A plot of log-normal variance of the optical signal against  $h^2$  is shown in Figure 14. The signal

samples are numbered from 3 to 43 for easy identification of any signal sample. The list of optical signal samples is contained in Appendix A.

From Figure 14, it can be seen that there is an apparent 'peak' in the signal fluctuations for signal samples 14 to 17. The higher signal fluctuations are due to the increased roughness of the ocean wind waves associated with the signal samples. The wave age, defined as the ratio of the ocean surface waves phase speed,  $C_p$  to the wind speed,  $u$  is a good measure of roughness of the surface waves. Donelan, et. al. [Ref 13], demonstrated that younger waves traveling slower than the wind are rougher than mature waves. A plot of the optical signal log-normal variance against wave age for signal samples 3 to 5 and 14 to 17 is shown in Figure 15. The plot indicates a decrease in signal fluctuations with increased wave age. However, signal samples 14 and 15 have higher signal fluctuations than samples 3 and 4 although they are associated with wind generated waves of approximately the same wave age. The higher fluctuations of samples 14 and 15 are due to the influence of the swell. The influence of the swell on sample 14 and 15 is manifested in the temperature fluctuations spectral densities where the swell frequencies modulate the temperature spectra. This effect is shown in Figures 16 and 17. The corresponding temperature spectra for samples 3 and 4 do not display any prominent peak in the swell frequencies. The temperature spectra and the ocean surface elevation spectra for samples 3 and 4 are shown in Figures 18 and 19. The presence of swell caused a change in the spectral distribution of the various components of the high frequency wind waves. There is experimental evidence that this leads to an increased in roughness of the ocean surface [Ref. 14].

Two alternative analyses were performed to verify the trend of the signal fluctuations. In the first method, it is assumed that the ocean surface elevation follows a Gaussian distribution,  $\eta(0,\sigma)$ . This is true for a sample with a large number of points. Based on the height of the ray path above mean sea level, the probability of ocean surface waves protruding into the ray path can be computed from

$$P(z > z_{ht}) = \int_{z_{ht}}^{\infty} \frac{1}{\sqrt{2\pi\sigma^2}} e^{-z^2/(2\sigma^2)} dz . \quad (69)$$

The percentage of the ocean waves protruding into the ray path is found by multiplying Equation (69) by 100. The percentage values are plotted against the signal log-normal variance. It was found that the signal fluctuations exhibit the same trend. A plot of the percentage of ocean waves protruding into the optical ray path is shown in Figure 20.

In the second method, the log-normal variance of the signal samples are plotted against the difference between the ray path height and one significant wave height above the wave crests. The same trend in signal fluctuations was observed. For signal samples that are less than one significant wave height above the ocean surface waves, the sample points are widely scattered as in the above two analyses. The plot is shown in Figure 21. The analyses led to the conclusion that the random motion of the ocean waves is affecting air turbulence

immediately above the ocean surface and causing increased variability in signal fluctuations as the ray path gets closer to the ocean surface.

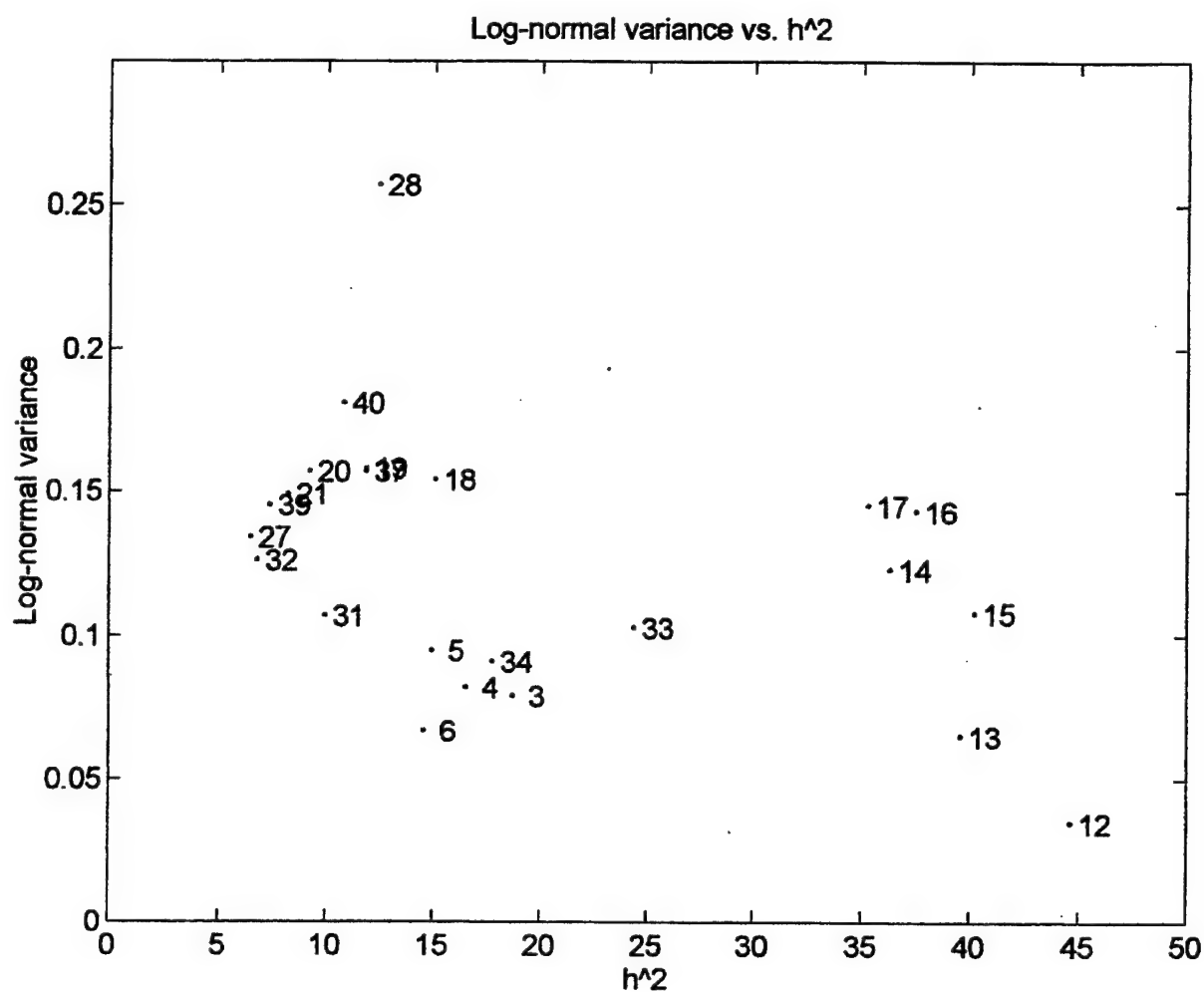


**Figure 14.** Log-normal Variance of Optical Signal vs.  $h^2$ .

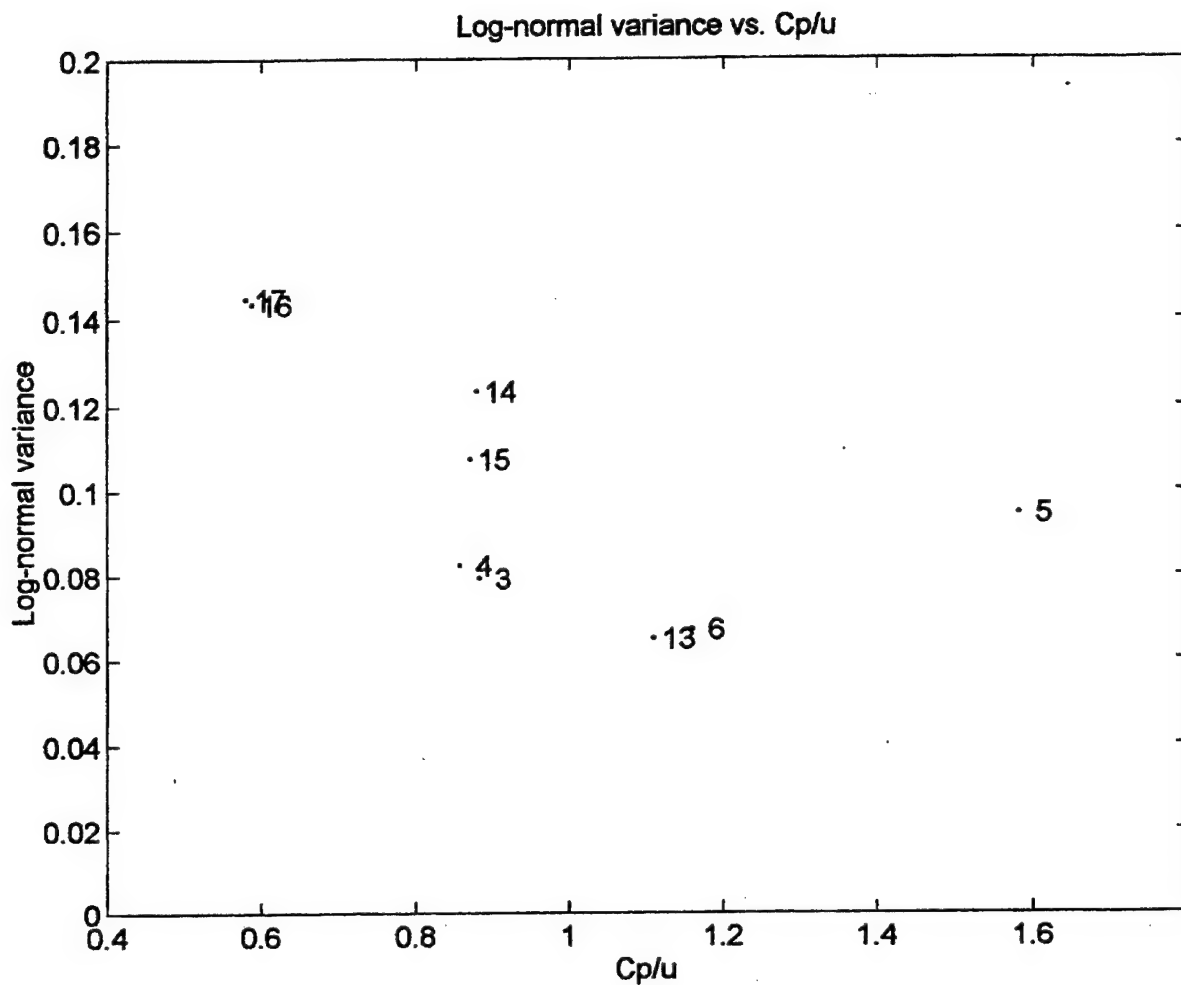


**Figure 15.** Optical Signal Log-normal Variance vs. Wind Wave Age.



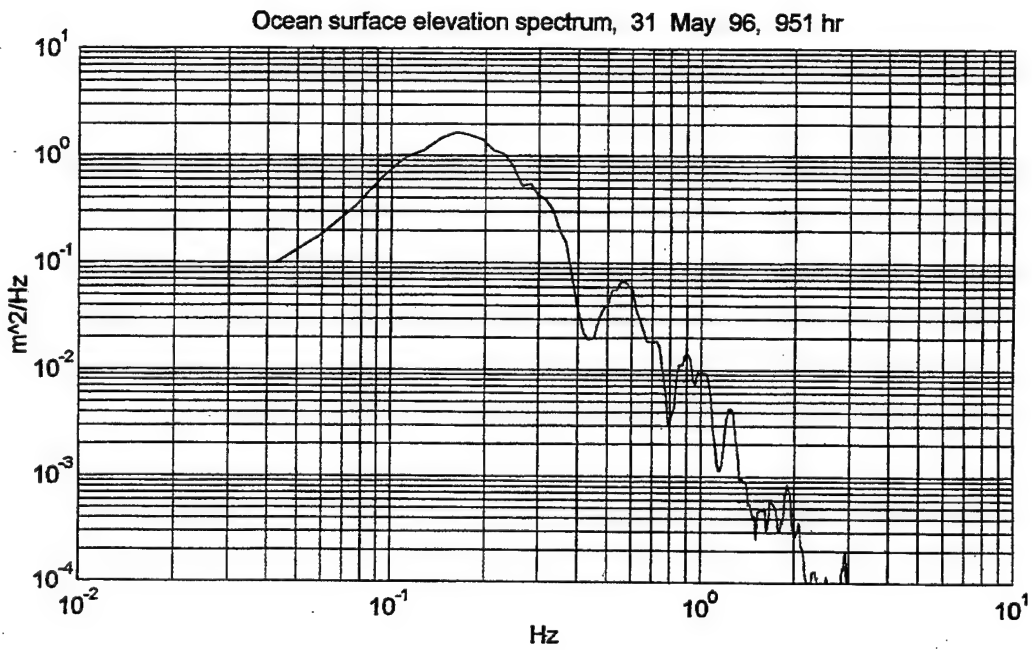
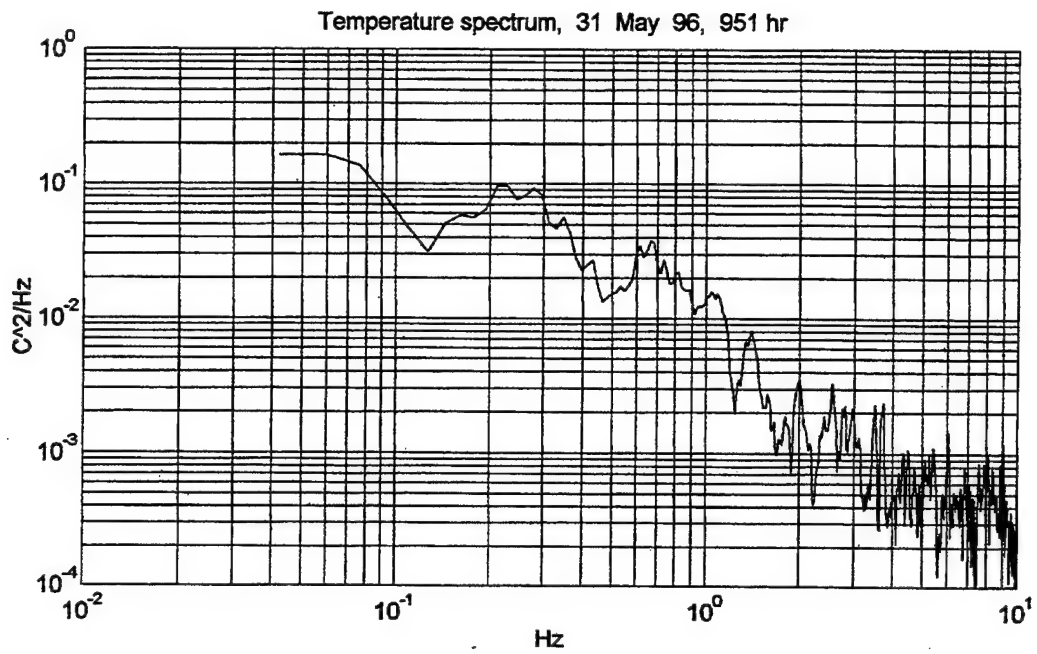


**Figure 16.** Optical Signal Sample No. 14, Temperature Spectrum and the corresponding Ocean Surface Wave Displacement Spectrum

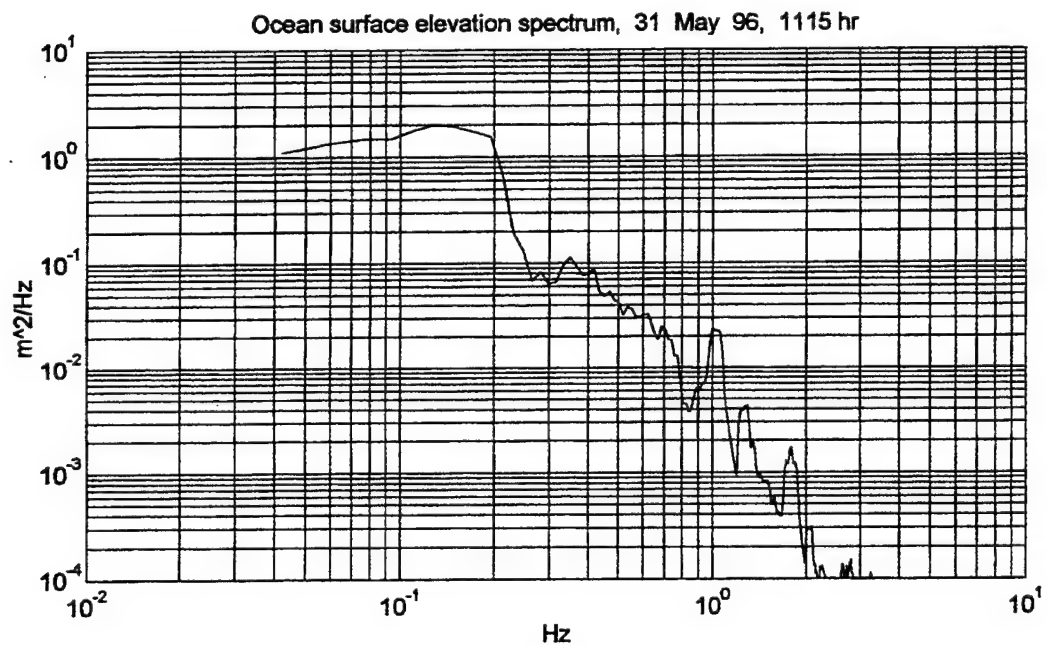
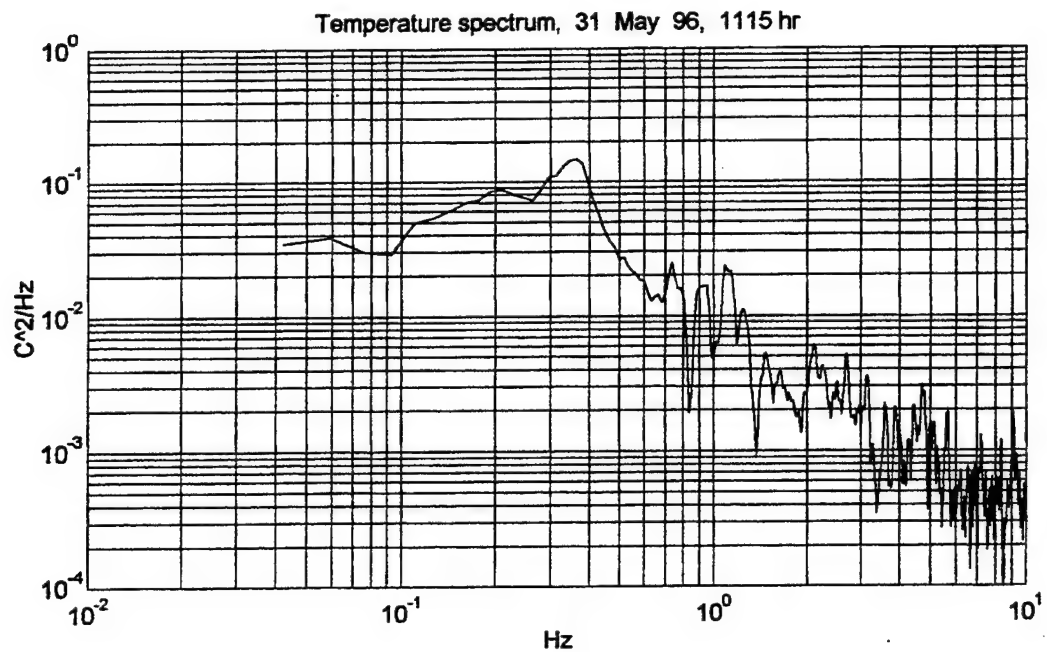


**Figure 17.** Optical Signal Sample No. 15, Temperature Spectrum and the Corresponding Ocean Surface Wave Displacement Spectrum.

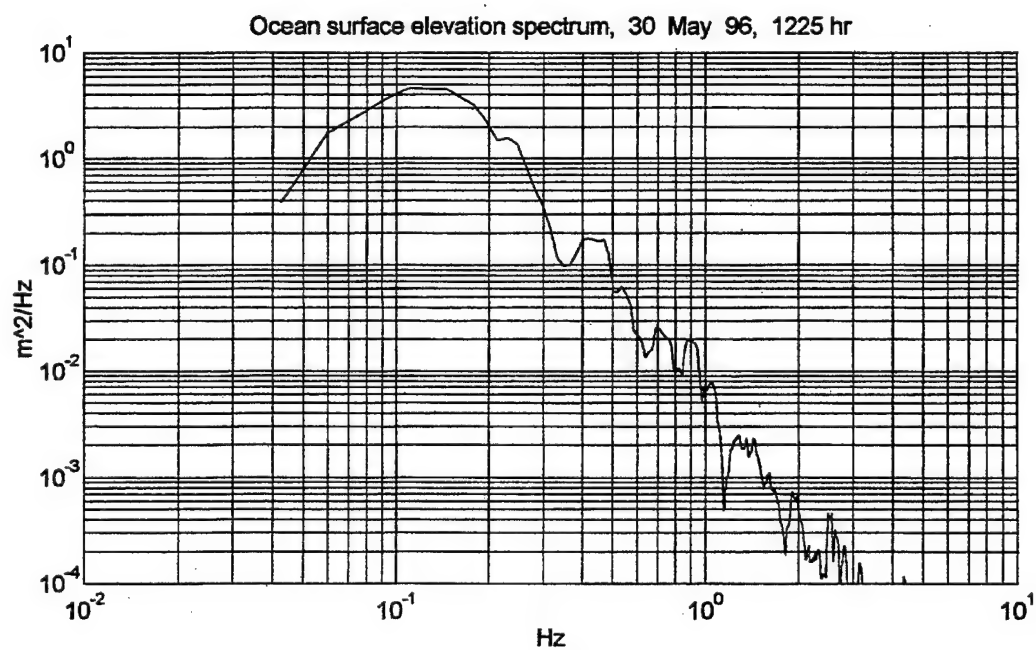
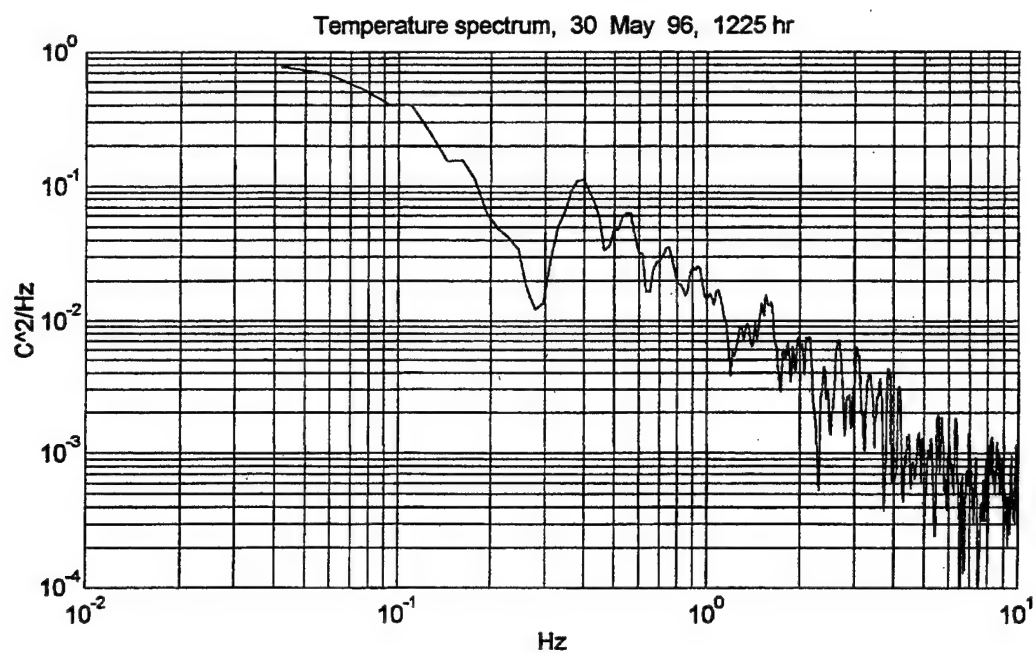


**Figure 18.** Optical Signal Sample No. 3, Temperature Spectrum and the corresponding Ocean Surface Wave Displacement Spectrum

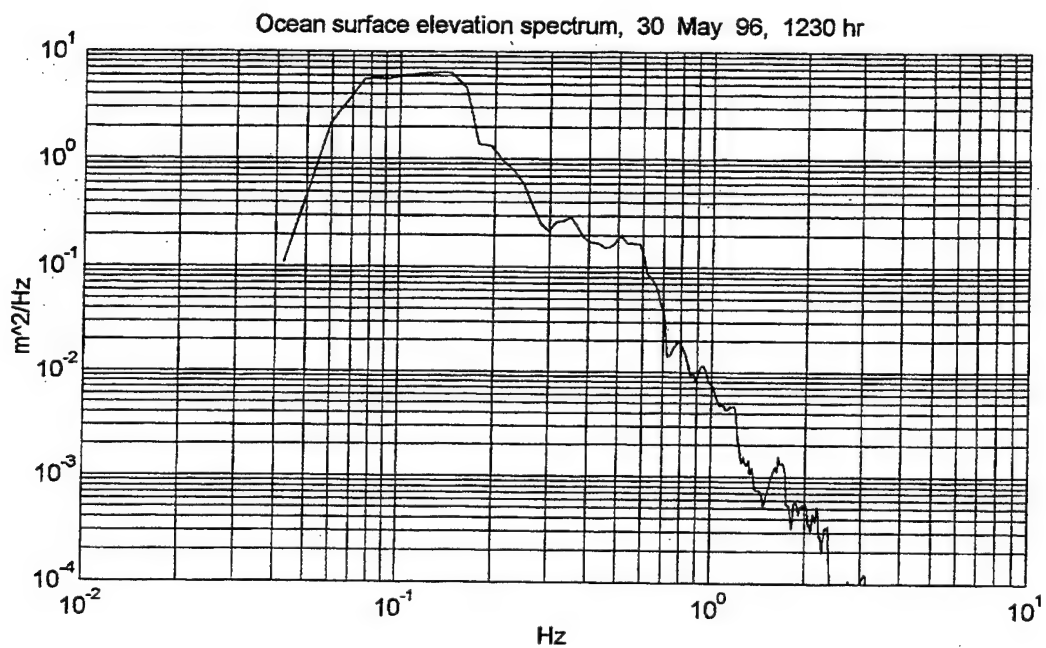
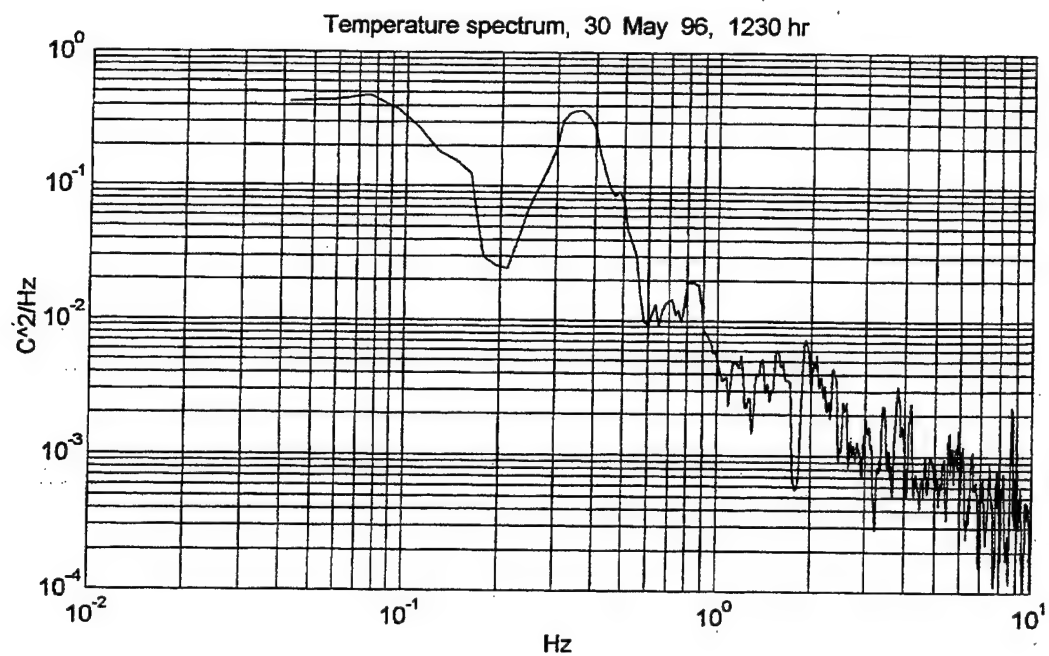


**Figure 19.** Optical Signal Sample No. 4, Temperature Spectrum and the corresponding Ocean Surface Wave Displacement Spectrum

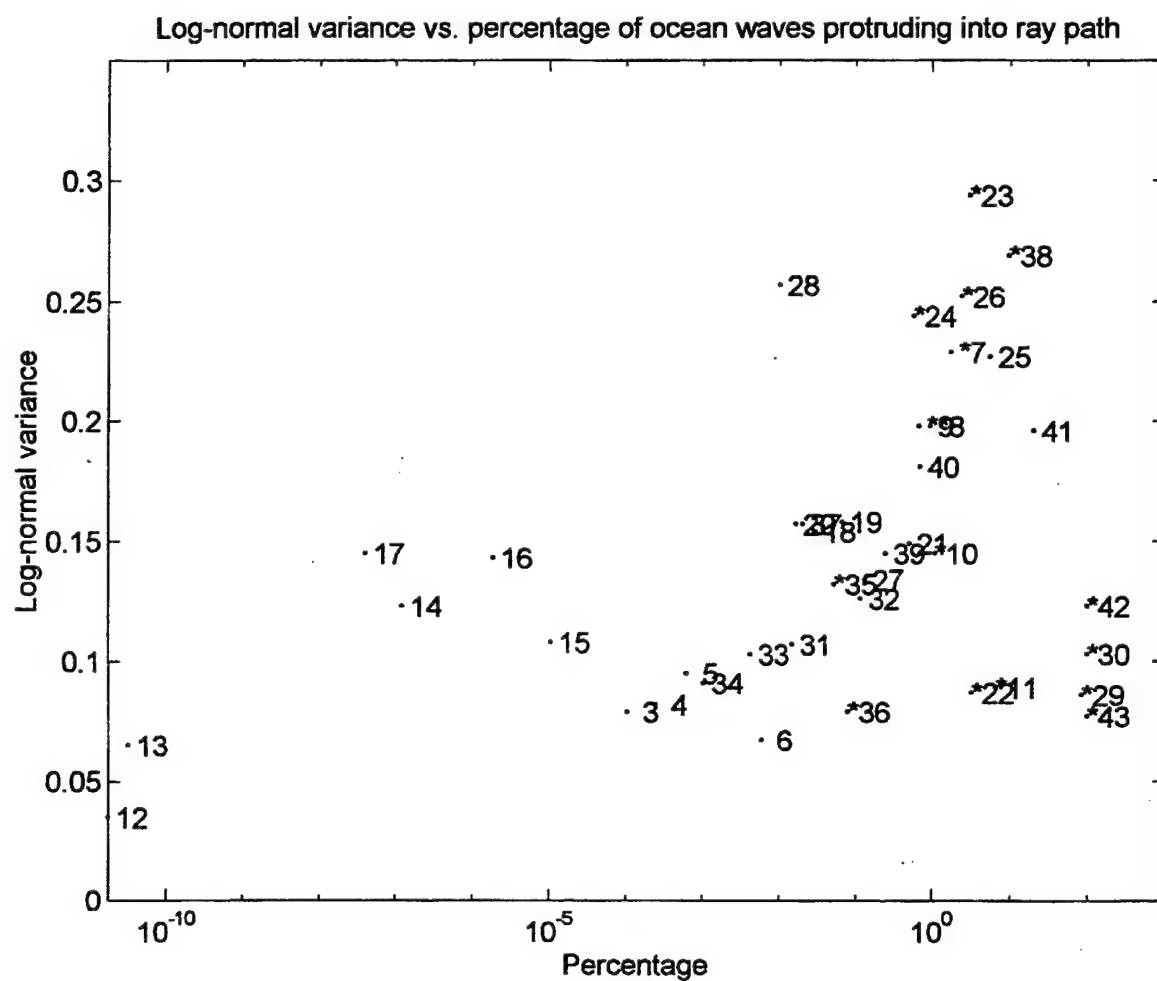


**Figure 20.** Percentage of Ocean Waves Protruding into Optical Ray Path.

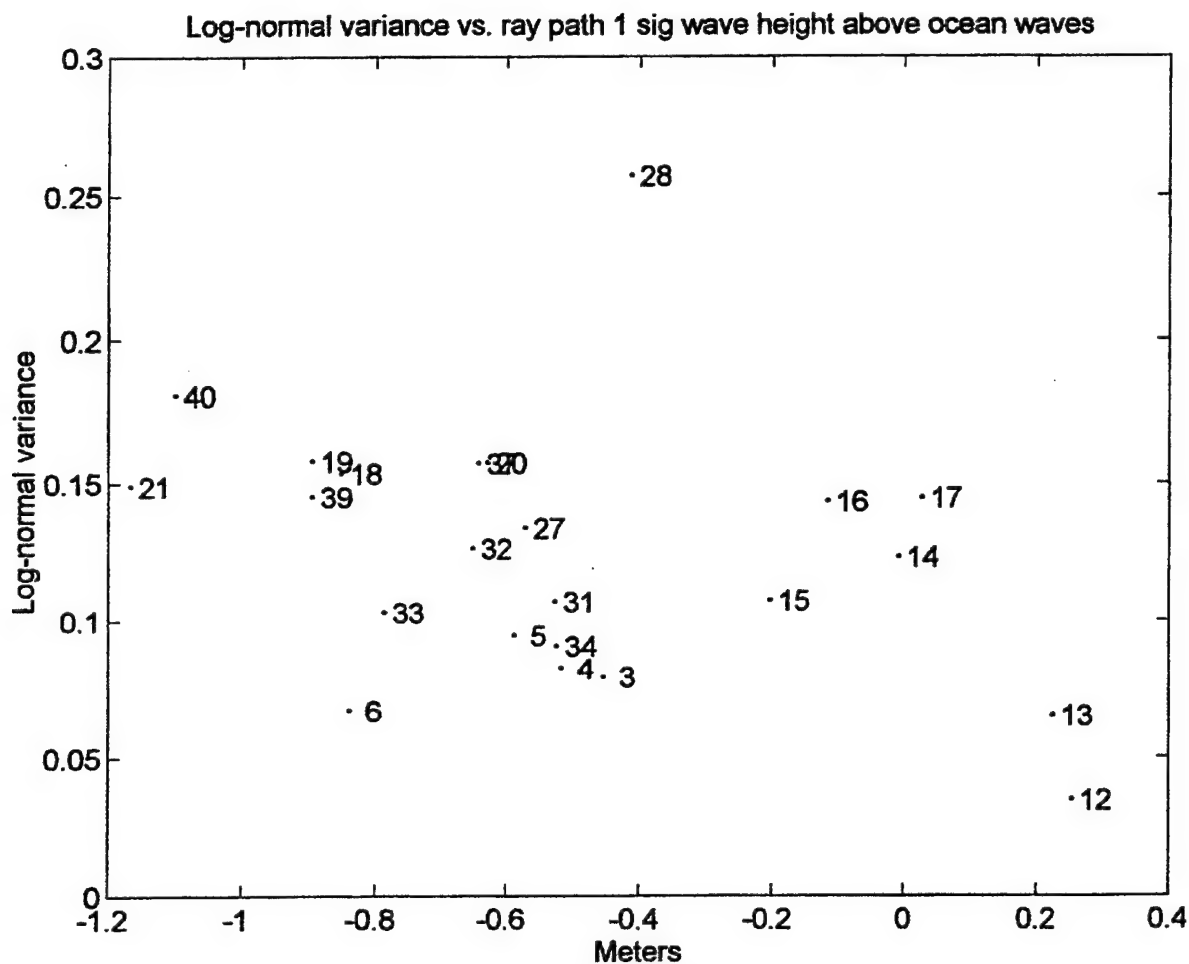


**Figure 21.** Log-normal Variance of Optical Signal vs. Ray Path 1 Significant Wave Height above Ocean Waves.

## **E. OPTICAL SIGNAL MODULATION BY OCEAN SURFACE WAVES**

The intensity spectrum for each optical signal sample was computed and compared with the corresponding ocean surface wave spectrum. The plot (Figure 22) shows that for optical signals that were partially occluded by the ocean surface waves, the optical signal spectrum displays peaks at the swell frequency of the ocean waves. The optical signal is said to be modulated by the ocean waves.

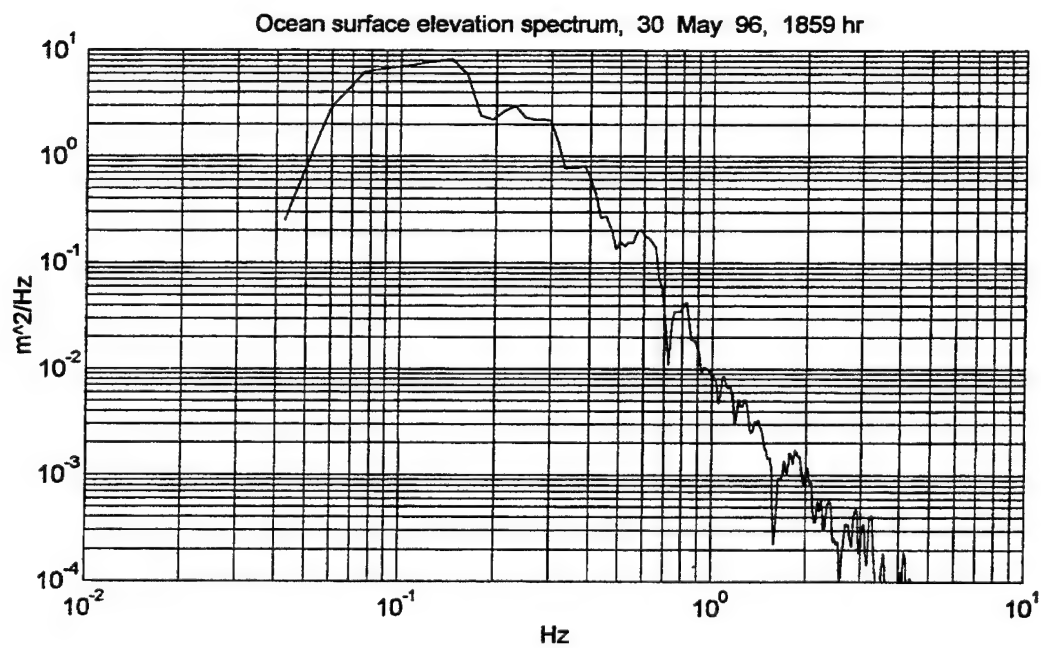
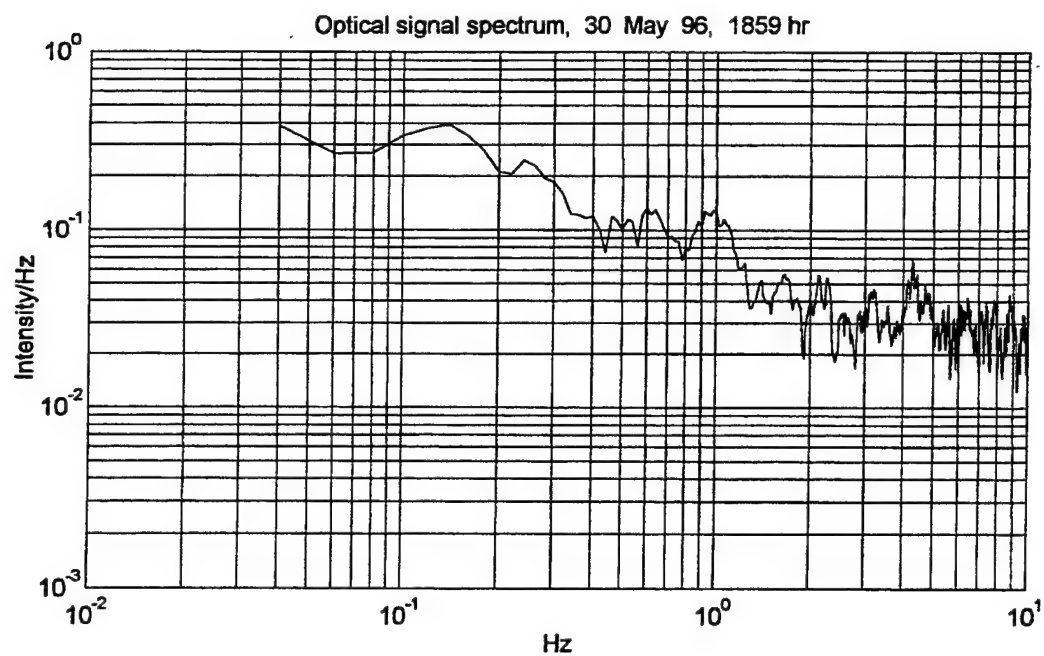


**Figure 22.** Optical Signal Spectrum and the Corresponding Ocean Wave Spectrum.



## **F. NEAR-SURFACE MEAN GRADIENTS**

In the above, only small-scale variations are considered whereby turbulence produces random fluctuations in the density of air and hence fluctuations in the refractive index. On larger scale variations, the main concern is on phenomena that affect the average position of the optical beam as it traverses the atmospheric medium. In the experiment, the effects of the ocean waves on vertical temperature profile and hence the refractive index profile is investigated.

There is evidence from the experiment that the air turbulence due to the ocean waves resulted in deviations of the vertical temperature profile from the logarithmic profile thereby affecting the refraction of the optical signals. To analyze the refraction of the optical signal, only samples of those above the ocean waves, i.e., those not occluded by ocean waves, were used. For each time sample, the corresponding transmitter and receiver heights above mean sea levels were calculated from GPS surveying data and tide measurements provided by a National Oceanographic and Atmospheric Administration tide gauge. With the measured transmitter and receiver heights, and using the standard logarithmic temperature profile in the ray tracing program, it was observed that optical continuity between the transmitter and the receiver could not be established. An example of the ray tracing plot is shown in Figure 23. The mechanism in which the ocean waves affect the index of refraction needs to be examined. This research attempts to relate the effects of ocean waves on the temperature profile using the mixing length concept.

The mixing length concept was introduced by Prandtl in 1925 to describe the

properties of turbulent transfer. In this model, it is assumed that there exists a length scale called the mixing length over which a turbulent eddy can travel and still maintain its identity. Details of the mixing length concept is contained in Appendix B.

The effects of ocean surface waves on the gradients of the vertical temperature profile are discussed in the next section.

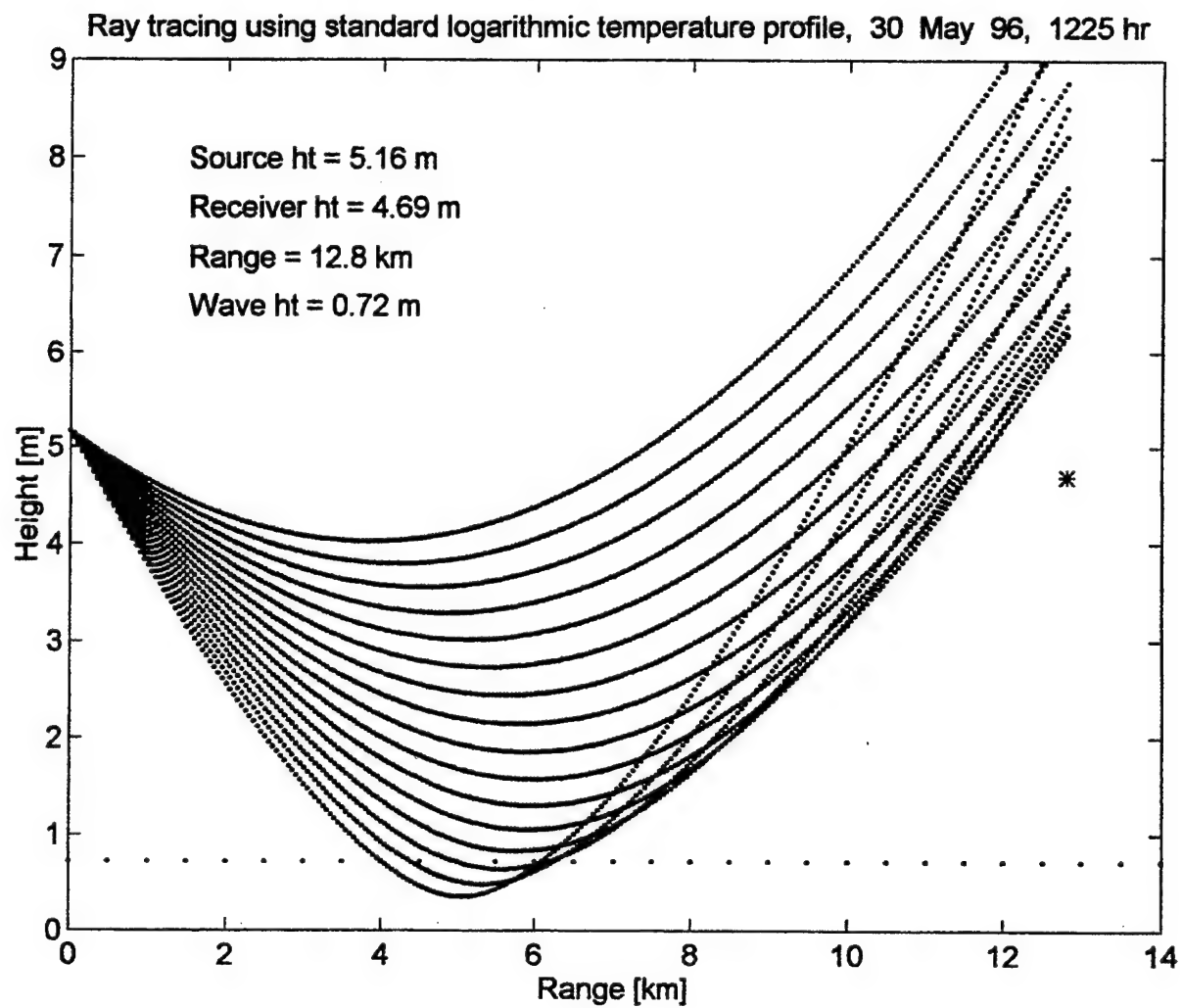


**Figure 23.** Optical Continuity cannot be established between Transmitter and Receiver.

## G. EFFECTS OF OCEAN SURFACE WAVES ON THE INDEX OF REFRACTION

The refractive index at optical frequencies can be approximated by

$$n-1 = 77.6(1+7.52 \times 10^{-3} \lambda^{-2})(P/T)10^{-6} , \quad (70)$$

where  $P$  is the atmospheric pressure in millibars,  $T$  is the temperature in Kelvin and  $\lambda$  is the wavelength of light in  $\mu\text{m}$ . In the atmospheric surface layer, pressure variation is small and can be neglected. Variation in the index of refraction is thus caused by the variation of temperature in the atmospheric surface layer.

The vertical profiles of wind speed,  $u$ , temperature,  $T$  and humidity,  $q$  all have logarithmic forms  $\xi = (u, T, q)$ , given by

$$\xi = \xi_s + \frac{\xi_*}{\kappa} \left[ \ln \left( \frac{z}{z_{0\xi}} \right) - \psi_\xi \left( \frac{z}{L} \right) \right] \quad (71)$$

and the gradient profile given by

$$\frac{\partial \xi}{\partial z} = \frac{\xi_*}{\kappa z} \phi_\xi \left( \frac{z}{L} \right), \quad (72)$$

where  $\xi_*$  is the flux scaling parameter,  $\xi_s$  is the value at the surface,  $z_{0\xi}$  is the roughness length,  $\kappa$  is the von Karman constant and  $\phi_\xi(z/L)$  is the derivative version of the stability functions given in Appendix B. In Equation (72), the term  $\kappa z$  is the turbulence mixing length.

The above profiles are derived for turbulence above an immovable surface. A distinctive feature of the boundary layer adjacent to the ocean surface is the presence of a continuous random movement of the ocean surface. The presence of the random varying air-wave interface produces a constant variation in resistance of the ocean surface. The roughness elements that originate from the various components of the wave spectrum contribute in varying degree to the total wave dispersion. The air flow above the ocean waves induces a pressure field which transfers part of the energy of the air flow to the waves during wave development or conversely, the waves transfer energy to the air during swell attenuation. The surface waves, on the other hand, disturb the air flow above them and form air waves which interact with the gradient of the vertical profile.

The wavy motion of the surface affects the profile deviation in two ways. Firstly, the short waves (high frequency component) contribute to the roughness of the water surface. The quantity  $z_{0u}$  specifies the scale of the turbulent eddies that are generated by the surface roughness elements. Experimental evidence [Ref. 16] suggested that surface roughness should be proportional to wave steepness,  $H/\Lambda$ , where  $H$  is the wave height and  $\Lambda$  is the wavelength

of the dominant ocean wind waves, i.e.,

$$z_{0u} \propto \frac{H}{\Lambda} \frac{u_*}{g} \quad (73)$$

As the ocean wave phase speed,  $C \propto [g\Lambda/(2\pi)]^{1/2}$ ,  $z_{0u}$  can be expressed as

$$z_{0u} = a \frac{H}{2\pi} \left( \frac{u_*}{C} \right)^2, \quad (74)$$

where  $a$  is the constant of proportionality. Equation (74) implies  $z_{0u} \propto H$  and  $z_{0u} \propto u_*$ . A large  $u_*$  implies a small  $T_*$  as

$$T_* \propto \frac{\overline{w'T'}}{u_*} \quad (75)$$

and hence a smaller temperature profile gradient. In Equation (75), the overbar refers to averaging over a suitable time period.

In this experiment, however, the wind speed was relatively low, with average wind speed of about 3.95 m/s. The dependence of roughness on wave steepness may be reduced. It may suffice to use Charnock's formula that has been interpolated to cover regime between

low wind and high wind speed [Ref. 16],

$$z_c = 0.0185 \frac{u_*}{g}, \quad (76)$$

where  $g$  is the gravitational acceleration and  $u_*$  is the friction velocity. The roughness length for a smooth surface is given by

$$z_s = 0.11 \frac{\nu}{u_*}, \quad (77)$$

where  $\nu$  is the dynamic viscosity of air. The total roughness length is given by

$$z_{0u} = z_s + z_c. \quad (78)$$

The roughness lengths  $z_{0T}$  and  $z_{0q}$  are given by

$$z_{0T} = 0.4 \frac{\nu}{u_*} \quad (79)$$

and

$$z_{0q} = 0.62 \frac{v}{u_*} \quad (80)$$

Secondly, the longer surface waves do not contribute directly to the roughness,  $z_{0u}$  but they distort the air flow immediately above the ocean surface and are responsible for the vertical displacement of the frame of reference. Furthermore, the presence of the longer waves causes a redistribution of wave energy and the slope density of the short waves. This in turn influences the direction of the mean stress vector by creating an anisotropic roughness field at the surface. The long waves strained the shorter waves, causing them to turn in the direction of the longer waves. Donelan [Ref. 17] showed that the presence of long, gentle swell propagating in the wind direction has a significant effect on the wind sea spectrum. There is also evidence that counter swell, propagating against the wind led to higher drag coefficients than those experienced in pure wind waves [Ref. 14]. Therefore the presence of swell will influence the turbulence of the air above it. By direct interaction with the air flow and due to the fact that swells travel faster than the wind, the swells will transfer momentum to the air flow above it and thereby enhance turbulent mixing. Since the random motion of the surface waves generate turbulence in the air above the surface waves and increase turbulent mixing, it is appropriate to employ a statistical mixing length scale that accounts for the increased mixing. The solution adopted here is to characterize the increased turbulence by an effective random mixing length scale that varies with the significant surface wave height,  $H_s$ .



The significant wave height is one of the common parameter that oceanographers use as a measure for the average height of ocean surface waves. It is defined as the average of the highest one-third waves. The vertical profile of  $\xi$  becomes

$$\xi = \xi_0 + \frac{\xi_*}{\kappa} \left[ \ln \left( \frac{z + H_s}{z_{0\xi}} \right) - \psi_\xi \left( \frac{z}{L} \right) \right] \quad (81)$$

and

$$\frac{\partial \xi}{\partial z} = \frac{\xi_*}{\kappa(z + H_s)} \phi_\xi \left( \frac{z}{L} \right) \quad (82)$$

Equation (82) indicates that the presence of ocean surface waves will reduce the profile gradient in a random manner that is determined by the surface wave height. An increase in wave height will lead to a reduction in the profile gradient.

With the modified temperature profile, it was demonstrated by the ray tracing program that optical continuity between the transmitter and the receiver can be established. This is shown in Figure 24. This approach is based on applying the presumed scaling for the near surface condition.

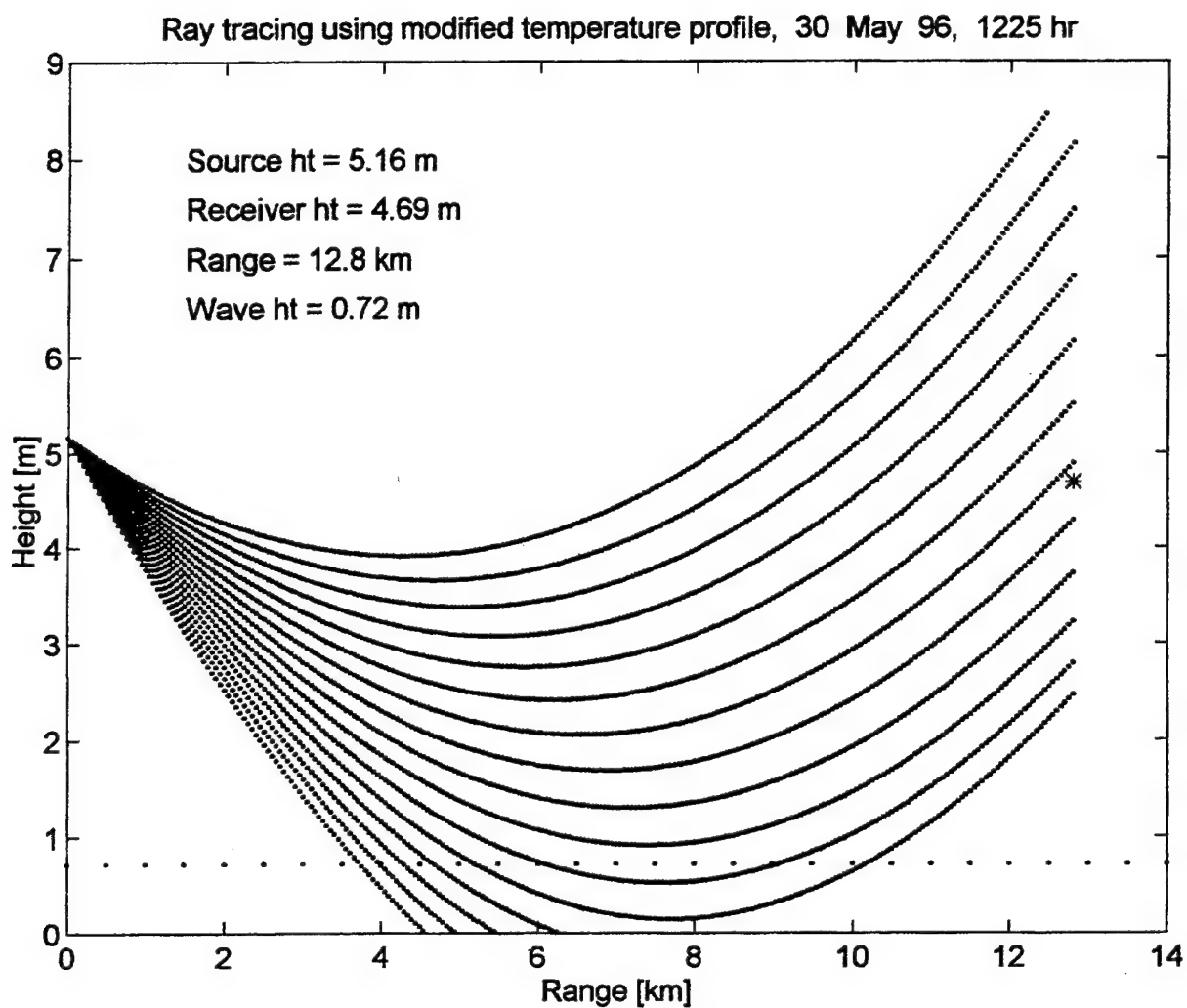


**Figure 24.** Ray Tracing with Proposed Temperature Profile. Optical continuity is established.

## VII. CONCLUSIONS AND RECOMMENDATIONS

This research showed that for optical signal samples that are not occluded by ocean surface waves, the signal fluctuations exhibit a log-normal distribution. This is characteristic of signals propagating through a random inhomogeneous medium. For signal samples that are occasionally obscured by ocean surface waves, the signal fluctuations deviate from a log-normal distribution.

The effects of ocean surface waves on optical signal fluctuations are revealed in the temperature fluctuation spectral densities. The temperature spectral densities display prominent peaks at the corresponding peak frequencies of the ocean surface waves. These characteristic peaks are not present in the temperature spectral densities computed from meteorological measurements over land.

Optical signal fluctuations increase as the signal ray path gets closer to the ocean surface waves demonstrating the significant effects of the ocean surface waves on signal fluctuations. Signal fluctuations were also shown to be dependent on wave age and the influence of ocean swells. Younger waves are rougher and are likely to cause a greater increase in signal fluctuations than more mature waves cause. When heights of signal samples are sufficiently low so that the ocean waves occasionally obstruct the ray paths, the ocean waves modulate the optical signals. Under moderate or high wind conditions, the ocean wind wave steepness should be incorporated into the roughness length scale,  $z_{0u}$ .

On larger scale variations, the ocean surface waves modify the vertical temperature

profile and hence the refractive index profile. The standard logarithmic temperature profile derived for meteorological conditions over land is not suitable for the marine environment above the undulating ocean surface. Ray tracing using the standard logarithmic temperature profile indicates that optical continuity could not be established between the transmitter and the receiver. Unlike conditions over land, the ocean waves distort the air flow above and increase turbulent mixing. This increased mixing is proportional to the ocean wave height. The increased turbulent mixing can be accounted for by incorporating a statistical mixing length proportional to the ocean wave height. The proposed temperature profile assures optical continuity between the transmitter and the receiver.

The research has demonstrated the significant effects of ocean surface waves on the propagation of low altitude optical signals above the ocean. The results of this study provide an insight into the effects of ocean surface waves on an optical signal skimming the ocean surface from an engineering view point. The study is not intended to disprove existing theories and hypotheses but rather to emphasize the relative importance of certain parameters that affect the propagation of optical signals in the vicinity of the ocean surface where the influence of ocean surface waves is significant.

The existing model (e.g. IR Tool) used by the Navy utilizes the standard logarithmic temperature profile to predict refraction of signals. The standard logarithmic profile is only valid for heights that are several significant wave heights above the ocean surface waves where the ocean wave effects are negligible. Within a few meters of the ocean surface waves, excessive ray bending occurs due to the logarithmic singularity of the temperature profile as

the ray approaches the ocean surface. The proposed statistical mixing length approach to modifying the temperature profile is perceived as an engineering fix to alleviate the large gradient in this critical layer above the ocean surface where sea-skimming threats are predominant. Further refinement in the modeling is recommended through extensive experimental measurements and data analysis. Modeling of signal propagation above an air-ocean interface spans an inter-disciplinary study of electronic engineering, oceanography and meteorology. The complexities of the air-ocean interface presents a unique challenge to scientists and engineers in a continuous search for more accurate modeling of signal propagation in this critical marine layer.



## **APPENDIX A. OPTICAL SIGNAL SAMPLES**

Optical Signal Samples

	A	B	C	D	E	F	G	H	I
1	Date time	Rx ht [m]	Tx ht [m]	height of	rms	%	h^2	log var	log var
2				ray path	wave ht				(wave occ)
3	5301225	4.69	5.16	1.71	0.36	0.000106	18.7128	0.079	
4	5301230	4.56	5.18	1.64	0.36	0.000248	16.5491	0.082	
5	5301233	4.41	5.19	1.57	0.36	0.00062	14.9584	0.095	
6	5301236	4.27	5.20	1.50	0.39	0.005863	14.5668	0.067	
7	5301838	4.44	4.94	1.47	0.7	1.789256	10.6063		0.229
8	5301843	4.26	4.91	1.36	0.58	0.956063	7.9751		0.198
9	5301859	3.86	4.82	1.11	0.45	0.688336	5.7584		0.198
10	5301903	3.77	4.80	1.05	0.46	1.123754	5.1516		0.145
11	5301909	3.59	4.78	0.94	0.63	6.725038	4.8771		0.089
12	5310943	4.40	4.95	1.45	0.2	1.78E-11	44.6558	0.035	
13	5310946	4.24	4.94	1.37	0.19	3.23E-11	39.5961	0.065	
14	5310951	4.15	4.93	1.31	0.22	1.22E-07	36.3271	0.123	
15	5311115	4.17	4.87	1.30	0.25	1.06E-05	40.2262	0.108	
16	5311120	4.10	4.88	1.27	0.23	1.88E-06	37.5196	0.143	
17	5311122	4.03	4.88	1.23	0.2	4.1E-08	35.2933	0.145	
18	5311830	3.86	4.87	1.13	0.33	0.030874	15.0818	0.154	
19	5311834	3.69	4.84	1.03	0.32	0.06726	11.8792	0.158	
20	5311836	3.53	4.83	0.93	0.26	0.016937	9.2211	0.157	
21	5311839	3.43	4.82	0.87	0.34	0.50895	8.2193	0.149	
22	5311932	2.94	4.55	0.48	0.26	3.26005	3.2021		0.087
23	5311937	3.07	4.53	0.54	0.29	3.116286	3.3635		0.294
24	5311948	3.32	4.47	0.66	0.26	0.586267	4.4495		0.244
25	6012208	3.22	4.05	0.41	0.26	5.780919	3.5517		0.227
26	6012243	3.21	4.03	0.39	0.2	2.511705	3.3162		0.252
27	6012308	3.53	4.05	0.57	0.19	0.134146	6.4756	0.134	
28	6021245	4.39	3.42	0.67	0.18	0.010306	12.4613	0.257	
29	6021417	2.43	3.59	-0.23	0.22	85.2618	3.0506		0.086
30	6021451	1.84	3.69	-0.52	0.2	99.52231	7.2935		0.103
31	6030930	4.01	4.01	0.79	0.22	0.015119	9.949	0.107	
32	6030937	3.81	3.96	0.67	0.22	0.117065	6.8136	0.126	
33	6031540	4.26	5.19	1.49	0.38	0.004213	24.3964	0.103	
34	6031551	3.83	5.23	1.28	0.3	0.001032	17.7704	0.091	
35	6031605	3.34	5.26	1.02	0.31	0.052834	11.5735		0.132
36	6031611	3.43	5.28	1.07	0.34	0.079321	13.1283		0.079
37	6041325	3.58	4.74	0.92	0.26	0.020864	11.8525	0.157	
38	6041417	2.77	4.68	0.44	0.34	9.854486	3.1197		0.269
39	6041426	3.38	4.69	0.79	0.28	0.249417	7.3583	0.145	
40	6051933	4.63	3.38	0.76	0.31	0.703241	10.8039	0.181	
41	6051945	3.42	3.40	0.20	0.24	20.57304	1.5127		0.196
42	6052000	1.69	3.42	-0.72	0.19	99.9921	8.4996		0.123
43	6052041	2.42	1.69	-1.17	0.22	99.99999	19.4317		0.077



Legend:

- Column A: Date and time of signal sample.
- Column B: Receiver height above mean sea level (in meters).
- Column C: Transmitter height above mean sea level (in meters).
- Column D: Lowest height of the ray path above mean sea level (in meters).
- Column E: Rms ocean wave height (in meters).
- Column F: Percentage of ocean surface waves protruding into optical signal ray path.
- Column G: Normalized mean square distance of optical signal ray path above ocean surface waves.
- Column H: Log-normal variance of signal samples not occluded by ocean surface waves.
- Column I: Log-normal variance of signal samples occluded by ocean surface waves. This is not strictly correct as the signal samples no longer exhibit log-normal distribution.



## APPENDIX B. MIXING LENGTH HYPOTHESIS

The mixing length concept was introduced by Prandtl in 1925 to describe the properties of turbulent transfer. In this model, it is assumed that there exists a length scale called the mixing length over which a turbulent eddy can travel and still maintain its identity.

Suppose, under neutral atmospheric conditions, a parcel of air moves vertically through a small distance,  $l$ , from its original position,  $z+l$ , where the characteristic quantity,  $q(z)$ , has an average value of  $\bar{q}(z+l)$ , then

$$q(z) \equiv \bar{q}(z+l) . \quad (83)$$

Using Reynold's decomposition,  $q(z)$  can be written as a sum of an average component and a fluctuating component,

$$q(z) = \bar{q}(z) + q'(z) . \quad (84)$$

Using mixing length hypothesis,

$$q'(z) = \bar{q}(z+l) - \bar{q}(z) \approx l \frac{\partial \bar{q}}{\partial z} . \quad (85)$$

Suppose  $\frac{\partial \bar{q}}{\partial z} > 0$ , then as shown in Figure 25,  $l > 0$  implies that the eddy comes from above and hence the vertical turbulent velocity,  $w' < 0$ . By the same token,  $l < 0$  implies

$w' > 0$ . The above argument indicates that  $l$  and  $w'$  are negatively correlated, i.e.,

$$\overline{w'l} < 0 . \quad (86)$$

Assuming that mixing length hypothesis applies to the turbulent velocity component and the air temperature then

$$T'(z) = l \frac{\partial \bar{T}}{\partial z} \quad (87)$$

and

$$u'(z) = l \frac{\partial \bar{u}}{\partial z} , \quad (88)$$

where  $T'$  is the turbulent air temperature and  $u'$  is the turbulent streamline wind velocity.

Equation (88) implies

$$\overline{w'u'} = \overline{w'l} \frac{\partial \bar{u}}{\partial z} . \quad (89)$$

In the atmospheric surface layer,  $\frac{\partial \bar{u}}{\partial z} > 0$  and since  $\overline{w'l} < 0$ , then

$$\overline{w'u'} < 0 . \quad (90)$$

Assuming the eddy velocity components,  $u'$  and  $w'$  have the same order of magnitude, then,

$$w' \sim u' \sim l \frac{\partial \bar{u}}{\partial z} . \quad (91)$$

Equations (89), (90) and (91) lead to

$$\overline{w'u'} = -l^2 \left( \frac{\partial \bar{u}}{\partial z} \right)^2 . \quad (92)$$

In the atmospheric surface layer, the mixing length varies with height above the earth's surface. Near the earth's surface, mixing cannot take place over large distances due to the solid boundary. Away from the surface, the turbulence is less inhibited and mixing is enhanced. In general, it is assumed that

$$l = \kappa z , \quad (93)$$

where  $\kappa$  is the von Karman constant.

In the atmospheric surface layer, the main task is to establish relationships between

vertical gradient of mean quantities of wind speed, temperature and specific humidity and surface fluxes. In particular, the surface fluxes of momentum,  $\tau$ , sensible heat,  $Q_H$ , and latent heat,  $Q_E$ , are given by

$$\tau = -\rho \overline{u'w'} = \rho u_*^2, \quad (94)$$

$$Q_H = \rho c_p \overline{T'w'} = -\rho c_p u_* T_* \quad (95)$$

and

$$Q_E = \rho L_e \overline{q'w'} = -\rho L_e u_* q_* \quad (96)$$

where  $c_p$  is the specific heat of air, and  $L_e$  is the latent heat of vaporization of water.

Combining Equations (92), (93) and (94),

$$\frac{\partial u}{\partial z} = \frac{u_*}{\kappa z}, \quad (97)$$

where  $u$  is the mean wind velocity (the overbar has been dropped for convenience). Similar equations for  $T$  and  $q$  can be written:

$$\frac{\partial T}{\partial z} = \frac{T_*}{\kappa z} \quad (98)$$

and

$$\frac{\partial q}{\partial z} = \frac{q_*}{\kappa z} \quad (99)$$

For non-neutral atmospheric conditions, Equations (97), (98) and (99) become

$$\frac{\partial u}{\partial z} = \frac{u_*}{\kappa z} \phi_u(z/L) , \quad (100)$$

$$\frac{\partial T}{\partial z} = \frac{T_*}{\kappa z} \phi_T(z/L) \quad (101)$$

and

$$\frac{\partial q}{\partial z} = \frac{q_*}{\kappa z} \phi_q(z/L) , \quad (102)$$

where  $\phi$ 's are the stability functions determined empirically,

$$\phi_u = \begin{cases} (1 - 20z/L)^{-1/4}, & z/L < 0 \\ 1 + 8z/L, & z/L \geq 0 \end{cases} , \quad (103)$$

$$\phi_T = \phi_q = \begin{cases} (1 - 16z/L)^{-1/2}, & z/L < 0 \\ 1 + 7z/L, & z/L \geq 0 \end{cases} \quad (104)$$

and  $z/L < 0$ ,  $z/L > 0$ , and  $z/L = 0$  correspond to unstable, stable and neutral stratification respectively and  $L$  is the Obukhov length.

Integrating equations (100), (101) and (102) yield profiles for mean  $u$ ,  $T$  and  $q$ ,

$$u = u_s + \frac{u_*}{\kappa} [\ln(z/z_{0u}) - \psi_u(z/L)] , \quad (105)$$



$$T = T_s + \frac{T^*}{\kappa} [\ln(z/z_{0T}) - \psi_T(z/L)] \quad (106)$$

and

$$q = q_s + \frac{q^*}{\kappa} [\ln(z/z_{0q}) - \psi_q(z/L)] , \quad (107)$$

where  $u_s$  ,  $T_s$  ,  $q_s$  are the values at the surface and  $\psi$ 's are the empirically derived stability correction functions given in Chapter V.

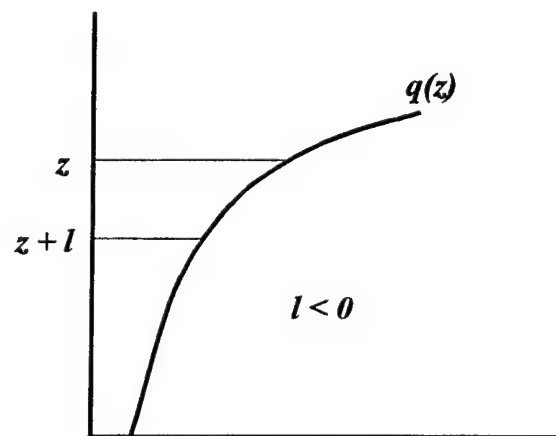
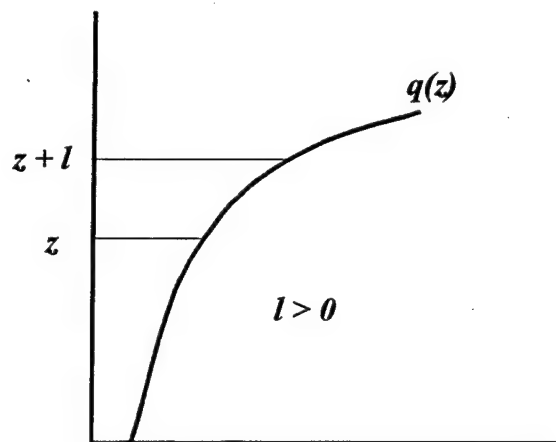


**Figure 25.** Mixing Length

## LIST OF REFERENCES

1. K. L. Davidson, G. E. Schacher, C. W. Fairall and A. K. Goroch, "Verification of the bulk method for calculating overwater optical turbulence," *Applied Optics*, vol. 20, No. 17, 1 September 1981.
2. Ed Takken, et al, "Observation of IR source at the ocean horizon," *Meeting of the IRIS Specialty Group on target background and discrimination*, 31 January - 2 February 1995.
3. B. A. Kagan, *Ocean-atmosphere interaction and climate modelling*, Cambridge University Press, 1995.
4. P. Schotanus, et al, "Temperature measure with sonic anemometer and its application to heat and moisture fluxes," *Boundary Layer Meteorology*, Vol. 26, 1983.
5. W. H. Lehn, "A simple parabolic model for the optics of the atmospheric surface layer," *Applied Mathematical Modelling*, Vol. 9, No. 6, December 1985.
6. W. M. Drennan, et al, "Directional Spectra from a Swath Ship at Sea," *Journal of Atmospheric and Oceanic Technology*, Vol. 11, August 1994.
7. F. Anctil, et al, "Eddy-Correlation Measurements of Air-Sea Fluxes from a Discus Buoy," *Journal of Atmospheric and Oceanic Technology*, Vol. 11, August 1994.
8. Private communication with Will Drennan.
9. F. Anctil, et al, "Deep-water field evaluation of the NDBC-SWADE 3-m discus directional Buoy," *American Meteorological Society*, Vol. 10, February 1993.
10. Y.A. Volkov, "The spectra of velocity and temperature fluctuations in airflow above the agitated sea," *Atmospheric and Oceanic Physics*, Vol. 5, No. 12, 1969.
11. G.R. Heidbreder and R.L. Mitchell, "Detection Probabilities for log-normally distributed signals," *IEEE Transactions on Aerospace and Electronic Systems*, Vol. AES-3, No. 1, January 1967.
12. P. Beckmann, "Amplitude-probability distribution of atmospheric radio noise," *Radio Science Journal of Research NBS/USNC-URSI*, Vol. 68 D, No. 6, June 1964.

13. M. A. Donelan, et. al., "On the dependence of sea surface roughness on wave development," *Journal of Physical Oceanography*, September 1993.
14. M.A. Donelan, et. al., "The air-sea momentum flux in conditions of wind sea and swell," *Journal of Physical Oceanography* [in press].
15. S. A. Hsu, "A dynamic roughness equation and its application to wind stress determination at the air-sea interface," *Journal of Physical Oceanography*, Vol. 4, 1974.
16. Anton Beljaars, "The parametrization of surface fluxes in large-scale models under free convection," *Q.J.R. Meteorol. Society*, Vol. 121, 1994.
17. M. A. Donelan, "The effect of swell on the growth of wind waves," *John Hopkins Applied Physics Laboratory Technical Digest*, Vol. 8, No. 1, 1987.

## INITIAL DISTRIBUTION LIST

		No. of Copies
1.	Defense Technical Information Center 8725, John J. Kingman Road, Ste 0944 Ft Belvoir, VA 22060-6218	2
2.	Library Naval Postgraduate School 411, Dyer Road Monterey, CA 93943-5101	2
3.	Department Chairman, Code EC Department of Electrical and Computer Engineering Naval Postgraduate School Monterey, CA 93943-5121	1
4.	Professor Hung-Mou Lee, Code EC/Lh Department of Electrical and Computer Engineering Naval Postgraduate School Monterey, CA 93943-5121	2
5.	Professor Richard W. Adler, Code EC/Ab Department of Electrical and Computer Engineering Naval Postgraduate School Monterey, CA 93943-5121	1
6.	Professor David C. Jenn, Code EC/Jn Department of Electrical and Computer Engineering Naval Postgraduate School Monterey, CA 93943-5121	1
7.	Professor Christopher Frenzen, Code MA/ Fr Department of Mathematics Naval Postgraduate School Monterey, CA 93943-5121	1

- |     |  |   |
|-----|--|---|
| 8.  | Professor Kenneth L. Davidson, Code MR/Ds<br>Department of Meteorology<br>Naval Postgraduate School<br>Monterey, CA 93943-5121 | 1 |
| 9.  | Lean-Weng Yeoh<br>59, Jalan Tari Serimpi<br>Singapore 799135<br>Republic of Singapore  | 2 |
| 10. | Library, CSO<br>Ministry of Defence, Singapore<br>c/o 59, Jalan Tari Serimpi<br>Singapore 799135<br>Republic of Singapore      | 2 |